In Vivo Monitoring and Magnetically-Enhanced Delivery of CAR T-Cells to Solid Tumor

Huan Chen, Alice Machado, Dongjie An, Sonia Becharef, Gwennhael Autret, Dmitry Ayollo, Sarah Razafindrakoto, Philippe Nizard, Florent Carn, Yun Luo, et al.

Article type: Full Paper

In Vivo Monitoring and Magnetically-Enhanced Delivery of CAR T-Cells to Solid Tumor

Huan Chen[1,5+], Alice Machado[2+], Dongjie An[2], Sonia Becharef,[1] Gwennhael Autret[4], Dmitry Ayollo[1], Sarah Razafindrakoto[1], Philippe Nizard[5], Florent Carn[1], Yun Luo[5], Frédéric Pendino[2], Claire Mangeney[5], Jelena Kolosnjaj-Tabi[3], Emmanuel Donnadieu[2], Florence Gazeau[1*]*

1 Laboratoire Matière et Systèmes Complexes MSC, Université Paris Cité, CNRS, Paris, France
2 Université Paris Cité, CNRS, Inserm, Institut Cochin, Equipe Labellisée Ligue Contre le Cancer. F-75014 Paris, France
3 Institute of pharmacology and structural biology, IPBS CNRS - UT3 Toulouse, France
4 Paris Cardiovascular Research Center PARCC, Université Paris Cité, INSERM, Paris, France
5 Laboratoire de Chimie et de Biochimie Pharmacologiques et Toxicologiques LCBPT, Université Paris Cité, CNRS, Paris, France

+ These authors contributed equally.

Corresponding authors: emmanuel.donnadieu@inserm.fr, florence.gazeau@u-paris.fr.

Keywords: CAR T-cell therapy, iron oxide nanoparticles, MRI, magnetic guiding, solid tumor.

Abstract

Chimeric Antigen Receptor (CAR) T-cell therapy demonstrated efficacy for the treatment of hematologic cancers, but remains challenging in solid tumors because of the hostile tumor microenvironment and heterogeneity that restrict the infiltration and activity of CAR T-cells. The lack of clinical imaging methods to monitor CAR T-cell therapy in patients limits the potential to enhance the therapeutic approach and predict patient response. Here we report a straightforward, non-invasive method for MRI tracking and magnetic targeting of CAR T-cells to enhance T-cell trafficking to solid tumors, in a setting that could be deployed in clinics. Iron oxide nanoparticles were loaded into T-cells, allowing MRI detection and magnetic cell guidance, while preserving T-cell viability, functions, and CAR specificity to target EGFR-expressing tumors. Longitudinal MRI monitoring of T-cells over 14 days revealed differences in tumor infiltration rates and antitumor efficacy between EGFR-targeted CAR T-cells and non-transduced T-cell. Moreover, an external magnet placed over the tumor enhanced the infiltration of CAR T-cells and increased their antitumor effect. MRI monitoring and magnetic guidance represent a dual-pronged clinically feasible therapeutic strategy to control and promote CAR T-cells delivery into solid tumors, thereby improving the precision, efficacy and safety of the treatment.

Introduction

Immunotherapy has recently emerged as the most promising therapeutic strategy to treat cancer. Immune cell-based therapies, in particular chimeric antigen receptor (CAR) T-cell therapy, are based on the genetic modification of patient T-cells to induce CAR expression on the cell surface and to specifically target tumor cells.[1,2] CARs are engineered receptors composed of an extracellular target antigen-binding domain, a hinge, a transmembrane domain, and several intracellular signaling domains that provide specificity and T-cell–activating functions.[3,4] The general premise for their use in cancer immunotherapy is to rapidly generate tumor-targeted T-cells and exert immediate and long-term effects.[5-7] Despite the success of CAR T-cell therapy in the treatment of advanced stages of hematologic cancers, there are still some drawbacks and resistance, especially in the context of solid tumors.[8,9] Various obstacles have been identified, including the poor T-cell infiltration and penetration in the hostile tumor microenvironment (TME).[10] Once within the tumors, engineered T-cells face a highly suppressive environment that has a negative impact on the response to CAR T-cell therapy.[10] Moreover, the heterogeneous antigen expression also plays a role in tumor escape to CAR T-cells. In addition to these flaws in efficacy, CAR-T-cells can also present several toxicities that include attack of healthy cells expressing the target even in very low amounts.[11] Thus, the selection of the antigen receptor in CAR T-cell design is a crucial aspect that influences the safety and efficacy of the therapy.[6,12,13] Balancing these considerations is a complex task that requires a deep understanding of the biology of both the target antigen and the surrounding TME. Epidermal Growth Factor Receptor (EGFR) has emerged as a prominent target in the development of anticancer therapies, particularly for lung cancer and various other malignancies, with both monoclonal specific antibodies and CAR T-cells targeting EGFR demonstrating clinical anti-tumor efficacy.[14-16] However, one critical challenge associated with EGFR-targeted therapies, including CAR T-cells, lies in the potential for toxicity to not-

cancerous cells that also express EGFR in normal tissues, including the skin, gastrointestinal tract, and certain epithelial cells.[17] To address these concerns, modifications may include the optimization of the binding affinity of the CAR for EGFR, incorporation of safety switches to enable the control of CAR T-cell activity, and implementation of sophisticated dosing regimens to manage potential side effects.[11] Hence controlling the biodistribution of CAR T-cells and their infiltration in different tissues including solid tumors is of utmost importance. In the context of solid tumors, we and others have shown that abnormal generation and organization of extracellular matrix, collagen crosslinking and stiffening of the stroma drastically reduce T-cell infiltration and make them unable to reach their target tumor cells.[18,19] Combinatorial strategies are thus needed to overcome the hostile TME and increase T-cell specificity and accumulation in solid tumors.[20] However the lack of imaging and longitudinal monitoring during CAR T-cell clinical use severely impedes the crucial collection of information to improve and modulate the treatment.[21,22] Longitudinal monitoring of CAR T-cell therapy would provide a dynamic approach allowing real-time tracking of T-cell infiltration, distribution, and cytotoxicity within the tumor or healthy tissues and subsequent adaptation of the treatment depending of the patient dynamic response.[23-25] Currently, the most common and mostly pre-clinical method for cell tracking is optical-based fluorescence (or bioluminescent) imaging.[26] The main advantages of this approach are that reporter genes continue to be expressed even after cell division and throughout the cell lifespan. However, optical imaging has several significant disadvantages, such as low tissue penetration of light, which hinders imaging of deep-seated body structures, and a lack of spatial resolution and quantification *in vivo.* These restrictions limit the translation of the mentioned imaging technique to clinics. Magnetic resonance imaging (MRI) has emerged as one of the most effective methods for clinical diagnosis and prognosis due to its non-invasiveness, high spatial resolution, lack of ionizing radiation, ability to contrast soft tissues and deep tissue imaging. Cell labeling with MRI

contrast agents, such as the non-toxic, easily assimilated superparamagnetic iron oxide nanoparticles (IONPs), has been shown pivotal for tracking transplanted cells in preclinical and clinical cell-based therapies providing longitudinal *in vivo* information about their integration and effectiveness.[27-30] In immunotherapy, it aids in understanding immune cell distribution and persistence, shedding light on treatment mechanisms.[25,31-34] IONPs, some of them being clinically approved as iron supplements for anemia treatment, have been shown to be well tolerated, intracellularly degraded and rapidly recycled by the natural iron metabolism.[35,36]

Furthermore, the incorporation of magnetic intracellular payloads enabling cell manipulability as an active targeting strategy to direct therapeutic cells to their tissular target adds an additional layer of precision to cell therapy.[37-42] This approach leverages the use of magnetic field gradients to guide and enhance the migration of therapeutic cells towards specific sites.

In this context, a very recent study reported on the use of magneto-acoustic guidance and actuation of CAR T-cells to improve CAR T-cell delivery into solid tumors.[41] Therein, surface-modified, click-conjugated magnetic particles engineered CAR T-cells were magnetically guided in a protocol relying on continuous exposure to electromagnetic coils. Sequentially, a tumor-fixed acoustic tweezer was used to propel CAR T-cells into the tumor. While the proposed approach is technically sophisticated, interventions which would prioritize clinical feasibility and offer patient and medical practitioner convenience in magnetic manipulation together with longitudinal *in vivo* tracking of CAR T cells are yet to be uncovered.

With this constraint in mind, we explored the potentiality of ultrasmall citrate-coated γ-Fe_2O_3 biodegradable IONPs to magnetically label CAR T-cells via non-specific endocytosis internalization, without loss of EGFR-directed CAR T-cell specificity and antitumor functionality, allowing both MRI longitudinal monitoring and magnetic targeting of EGFR CAR T-cells towards human lung tumor xenograft in mice (**Scheme 1**). The migration, fate and

tumor control ability of EGFR CAR T- versus the non-transduced T-cells were followed longitudinally by whole body and high-resolution MRI tumor imaging at different time intervals up to 14 days after administration. Furthermore, we harnessed the magnetic properties of intracellular IONPs to increase the accumulation of CAR T-cells at the tumor site through the application of an external magnet placed over the tumor mass, resulting in enhanced antitumor efficiency. The magnetic guidance not only facilitates a more directed and efficient infiltration of T-cells into the tumor microenvironment at early time points but also offers the potential for clinically applicable spatial and temporal control over the therapeutic intervention. With the aim to overcome common resistance of solid tumors to cellular immunotherapy, our study uniquely combines two strategies of T cell targeting - antigen specific targeting and physical magnetic guiding - and a companion test, non-invasive MRI monitoring, in clinically applicable sequential procedures.

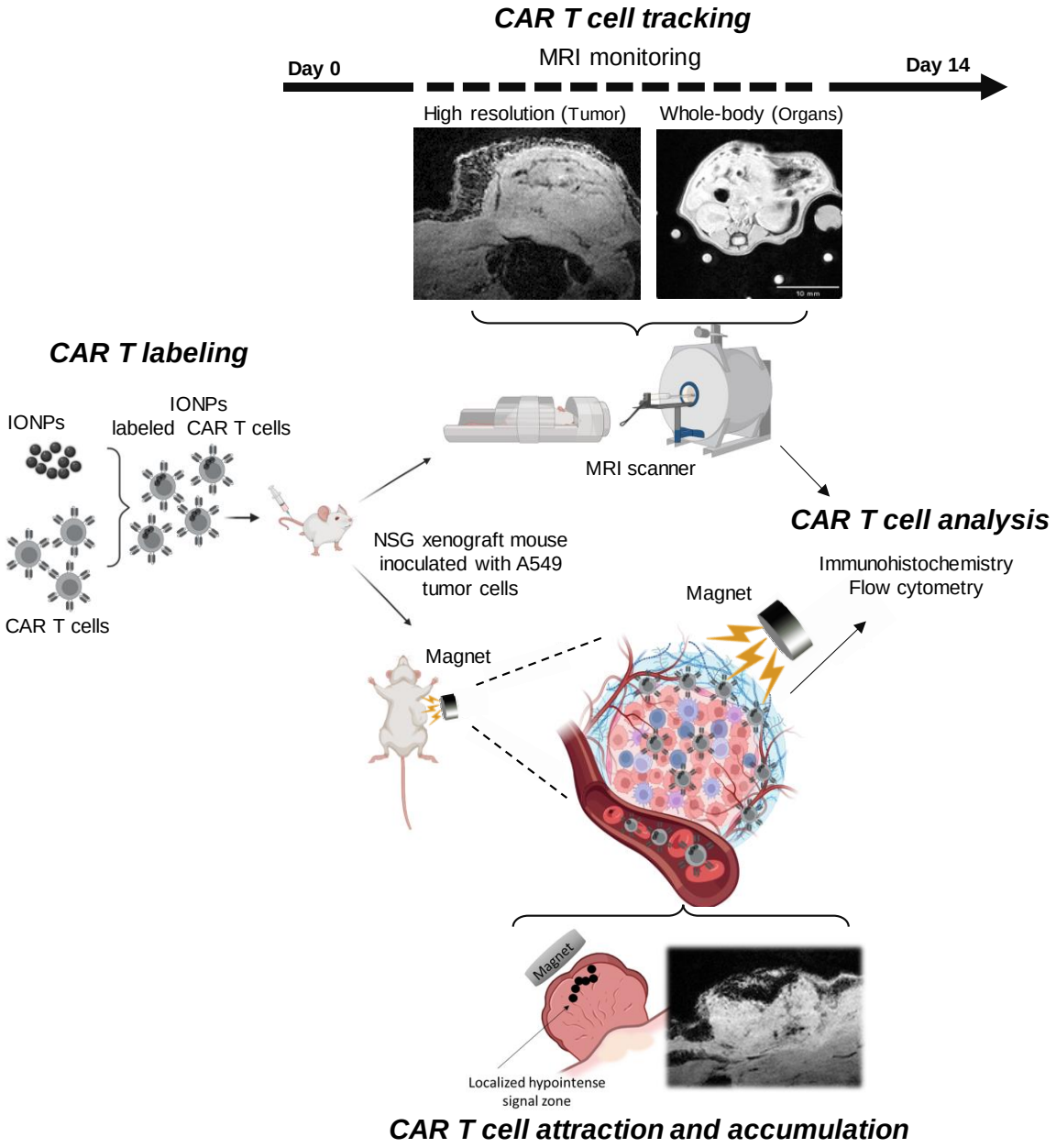

Scheme 1. EGFR CAR T-cells were loaded with IONPs *in vitro* and then intravenously injected into NOD scid gamma (NSG) mice bearing subcutaneous human lung cancer cell-derived xenograft. The longitudinal tracking of CAR T-cells action, in comparison to untransduced T-cells, was performed *in vivo* using both whole-body and high-resolution MRI over 14 days. In addition, an external magnet was used to promote early CAR T-cell guidance to the tumor and enhance antitumor efficacy.

2. Results and Discussion

CAR T-cells are efficiently and safely labeled with citrate-coated γ-Fe_2O_3 IONPs synthetized by coprecipitation, allowing MRI detection

Water dispersible citrate-coated spherical iron oxide maghemite nanoparticles (IONPs) obtained by the co-precipitation method (γ-Fe_2O_3 NPs, Massart's procedure[43]) were used in this study to label T-cells. Coprecipitation method is a green synthesis method (without need of organic solvents) with high yield, low cost, high product purity, high colloidal stability, reproducibility and scalability. The citrate-coated negatively-charged γ-Fe_2O_3 IONPs exhibit roughly spherical shapes and polydisperse diameters as seen on transmission electron microscopy (TEM) image in **Figure S1A.** The mean crystal diameter determined from TEM analysis is 7.4 nm, whereas the mean hydrodynamic diameter determined by dynamic light scattering (DLS) is of 26 nm, accounting for a solvation layer at the surface of the IONPs and possibly occurrence of small clusters in water suspension (**Figure S1A-B)**. Citrate-coated γ-Fe_2O_3 NPs have previously been demonstrated as highly efficient, safe, and inert magnetic labels readily internalized through non-specific endocytotic pathway for a diverse range of cells,[44] including lymphocytes with a specific T-cell receptor.[45,46]

Here magnetic cell labeling was initially tested on two different human T-cell lines, CEM and J77 (**Figure S2**), incubated with concentrations of IONPs ranging up to 200 µg/mL. Five mM sodium citrate was added in serum free RPMI medium to ensure IONP colloidal stability in the incubation medium as described earlier,[44] showing excellent IONPs biocompatibility during these labeling conditions. Mitochondrial metabolic activity assessed through the Alamar blue test in two human T cell lines was more than 90% of the non-labeled control cells for cells labeled with IONP concentration up to 50 µg/mL for two hours (**Figure S2A**). Consistently, the cell proliferation rate and viability evaluated at day 1, 3, 5, 7, and 9 post-labeling were comparable to the non-labeled cells for IONP concentration up to 50 µg/mL (**Figure S2B**).

Given these encouraging results on T-cell lines, we next assessed this magnetic labeling procedure on primary non-transduced T-cells (UNT T-cells) isolated from human blood, as well as on corresponding engineered EGFR-directed CAR T-cells (EGFR CAR T-cells). Briefly, resting primary T-cells were isolated from human peripheral blood mononuclear cells (PBMC) and stimulated with IL-2 and T-cell TransAct™ via CD3 and CD28 to induce activation and expansion of human T-cells. EGFR CAR T-cells were generated from activated T-cells using the plasmid construct encoding under EF-1alpha promoter for second-generation anti-EGFR CARs (from Nimotuzumab, a specific monoclonal antibody), CD8 hinge transmembrane domains, 4-1BB costimulatory, CD3z signalling domains. The plasmid also codes for enhanced green fluorescent protein (EGFP) to assess the percentage of transduction. Lentiviral particles were first produced in HEK293T packaging cell line and activated T-cells were transduced at day 1 and maintained in culture up to 12 days. CAR expression on the T-cell surface was quantified by flow cytometry using two different methods: first by measuring the percentage of EGFP co-expressed with the CAR and second by antibody staining using a biotinylated antibody specific to the extracellular domain of the human EGFR CAR. The results depicted in **Figure S3** demonstrate that over 60% of transduced T-cells express EGFP and are positive for anti-CAR staining. In contrast, non-transduced UNT T-cells show less than 1% EGFP expression and less than 4% anti-CAR positivity. These findings confirm efficient CAR expression in transduced T-cells, consistently co-expressing EGFP and the CAR. It must be noted however that the percentage of cells with CAR expression may vary depending of the donor, ranging from 30% to 65% in our experiments.

To achieve magnetic labeling of the primary T-cells, UNT T-cells and EGFR CAR T-cells were incubated with IONPs at varying concentrations ranging from 5 to 400 µg/mL for durations of 2 h and 24 h. The cell mitochondrial metabolic activity was thus assessed by Alamar blue test. The cell viability, determined as the percentage of the mitochondrial metabolic

activity of the cells non-exposed to IONPs, was not significantly affected after 2 h incubation (**Figure 1A**). However, when increasing the incubation time to 24 h (**Figure S4)**, the cell viability decreased drastically for both not-transduced and transduced T-cells probably because of nanoparticle late aggregation in the incubation medium. Based on our previous results with citrate-coated IONPs showing rapidly saturating nanoparticle uptake in various cell types,[44] we investigated the kinetics of IONP uptake by UNT T-cell for incubation times up to 4 h both at 4°C and 37°C (**Figure 1B**). Quantification of IONPs in cells was achieved by electron paramagnetic resonance (EPR) measurements as we reported earlier.[47] This quantification is based on the ferromagnetic resonance phenomena of IONPs, with an EPR absorption resonance spectrum characteristic of their superparamagnetic properties, size and magnetic anisotropy, as shown in **Figure S1D** for IONPs in colloidal suspension. After subtraction of the background EPR signal of the tube (**Figure S1C**) and double integration of the EPR spectrum, the total absorption signal is linearly proportional to the iron mass in the tube (**Figure S1E**) which provides a calibration curve. After uptake in the T-cells, the characteristic ferromagnetic resonance spectrum of IONPs (subtracted with the background EPR spectrum of non-labeled T-cells shown in **Figure S1C**) is slightly broadened due to magnetic interactions between IONPs in cells as shown in **Figure 1B** (left). Double integration provides a quantitative measurement of the average IONP mass per cell, shown in **Figure 1B** (middle). IONP uptake by UNT T-cells from two different donors consistently increases with incubation time but saturates after 2 h to a plateau that is larger at 37°C compared to 4°C. In another experiment with T-cells from a third donor, the IONP uptake reaches 4.9±0.7 pg (corresponding to approximatively 1.7 million of IONP per cell) and 8.9±0.5 pg per cell for 2 h incubation at 37 °C, with a bulk concentration of 50 μg/mL and 100 μg/mL IONPs, respectively (**Figure 1B** (right)). These consistent quantitative results in three T-cell donors are in full agreement with the mechanism of IONP uptake previously described[44] in different cell types. First, the

negatively-charged citrate-coated IONPs rapidly bind to the plasma membrane through non-specific electrostatic adsorption in the form of clusters, an adsorption step that occurs both at 4°C and 37°C. Second the plasma membrane invaginates only at 37°C allowing IONPs to be internalized by endocytosis pathway and to be confined in a couple of hours, successively into early endosomes and late endosomes, that fuse with lysosomes to concentrate the nanoparticles within intracellular compartments. This rapidly saturating IONP uptake is thus larger after incubation at 37°C compared to 4°C due to inhibition of the endocytosis process at 4°C, as confirmed by our quantitative results. TEM confirmed IONPs internalization within endo-lysosomes in both UNT T-cells and EGFR CAR T-cells soon after 2 h incubation. Indeed, TEM micrographs of 70 nm-thick sections of cells in **Figure 1C** illustrate some endo-lysosomes containing numerous IONPs. Of note, we previously gathered evidence on the degradability of IONPs in the acidic microenvironment of lysosomes and iron recycling into ferritins, the iron storage proteins, over long time periods (typically a few weeks).[48]

We next assessed the MRI detection of T-cells labeled with IONPs *in vitro*. When T-cells were dispersed in agarose gels, high resolution MR imaging with T2*-sensitive sequence revealed punctuate hypointense signals, visible as hypointense signal dots, in a cell density-dependent manner for IONPs-labeled T-cells (2 h incubation with 50 µg/mL IONPs), while agarose gels with control non-labeled T-cells exhibited a homogeneous hyperintense signal (**Figure 1D**). The number of signal voids in the MRI scans of each agarose gel was quantified, closely matching the total number of cells in the gel (**Figure 1E**). Of note, the MRI signal void created by each labeled cell, affecting a few voxels of 50 µm size, is much larger than the cell itself because it represents the spatially spreading relaxing effect on the proton magnetization of the magnetic field inhomogeneity created by the labeled cell, as detailed in our previous report.[45] This indicates that single T-cell detection could be achieved in agarose gels when γ-Fe_2O_3 IONPs were used as magnetic intracellular tag, labeling about 100% of the T-cells.

In addition, in order to investigate the influence of labeling IONP concentration on MRI cell detectability, we conducted additional *in vitro* MRI of agarose gels containing a fixed number of cells (15000), but labeled for 2 h using various bulk IONPs concentrations (50, 100 and 200 µg/mL). Comparable number and size of punctuate signal voids, reflecting the actual number of cells, were observed for the three IONPs labeling concentration (**Figure S5**), showing no advantage of increasing IONP concentration. Consequently, we adopted a labeling IONP concentration of 50 µg/mL and an incubation time of 2 h for our subsequent experiments, which represent a cost- and time-effective experimental work flow that could be easily translated in a clinical set up at the end of the CAR T manufacturing process.

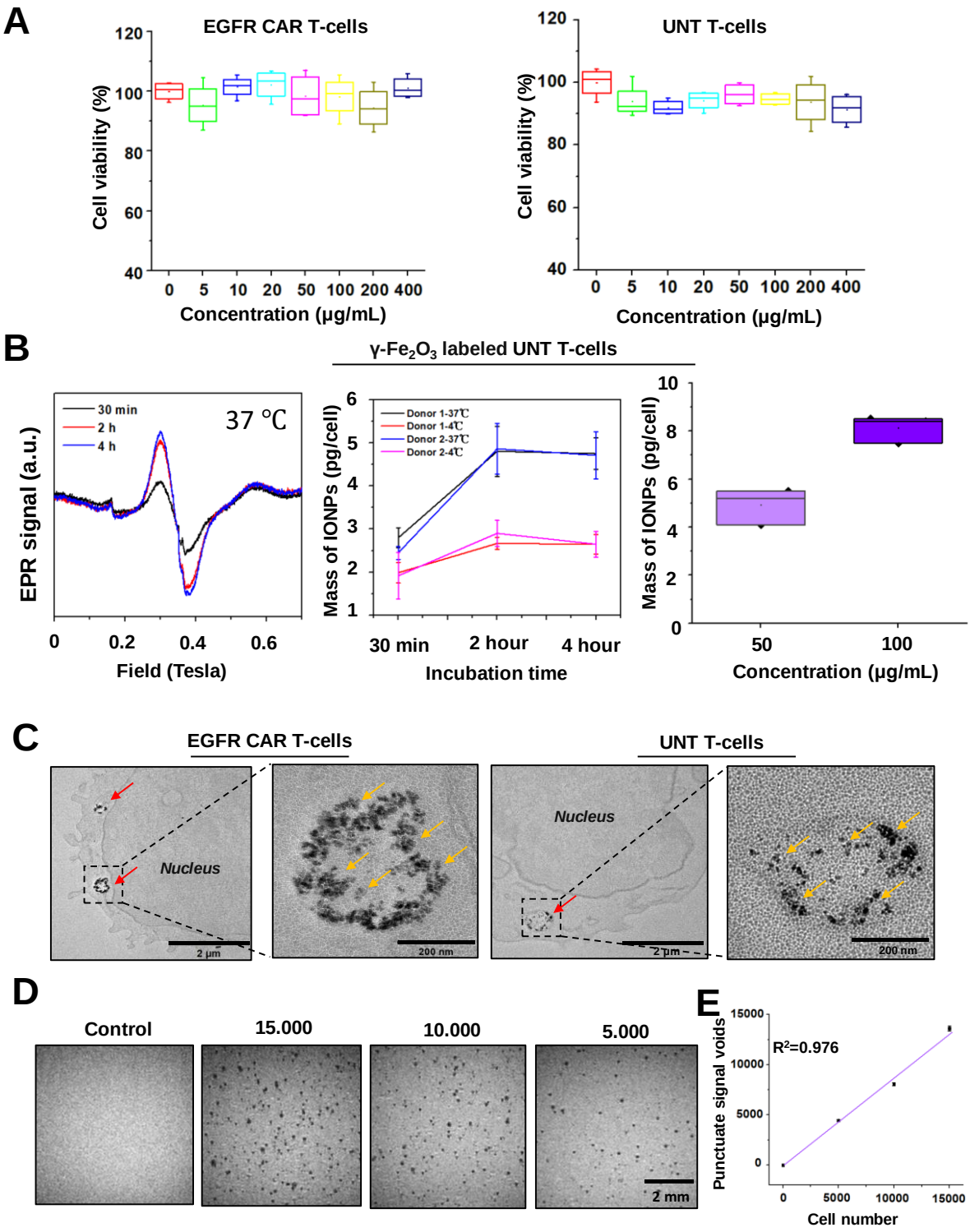

Figure 1. A) Percentage of cell viability assessed through the measurement of mitochondrial metabolic activity (normalized to the control cells non exposed to IONPs) with the Alamar blue test for UNT T-cell and EGFR CAR T-cell incubated for 2 hours with IONPs at different concentrations. B) from left to right: EPR spectra (subtracted from the cell EPR background

shown in Figure S1C) (left) and EPR quantification of IONP mass per cell (middle) for two donors of UNT T-cells incubated with IONPs at 50 µg/mL for 30 min, 2 h and 4 h, at 4°C or 37°C; EPR quantification of IONP mass per cell for UNT T-cells from a third donor incubated with IONPs at 50 µg/mL or 100 µg/mL for 2h at 37°C (right). C) Representative TEM micrographs of UNT T-cell and EGFR CAR T-cell after IONPs incubation for 2 h at 50 µg/mL. Representative whole cells (left panel micrographs, with red arrows pointing to IONPs-containing endo-lysosomes) and corresponding magnifications (right panel, with yellow arrows pointing to numerous endocytosed IONPs) illustrate intracellular endosomal confinement of IONPs within UNT and CAR T-cells. D) High resolution MR scans of agarose gels containing different number of T-cells labeled with IONPs concentration of 50 µg/mL for 2 h. 5000 to 15000 cells were dispersed in 500 µL of 0.3% agarose gels. Control is 0.3% agarose gel containing 15000 non-labeled cells. Spatial resolution is 50x50x50 μm^3. E) Punctuate signal voids (measuring between 5 and 100 voxels of 50x50x50 μm^3) were counted in four different fractions of the agarose gel, in a volume of 3 µL, and the mean including the standard deviation (SD) was normalized to the total 500 µL of gel. According to the linear regression line, the number of total signal voids matches the nominal number of T-cells dispersed in the gel, indicating single cell MRI detection. Results are representative of N=2 independent experiments, each containing n=3 replicates, and values are represented as mean ± SD.

IONPs-labeled T-cells are attracted towards a magnet

We then aimed to evaluate the influence of a magnetic field gradient generated by a magnet (described in **Figure S6**) on the retention of IONPs-labeled T-cells in culture medium (**Figure 2A**). Employing an *in vitro* dynamic flow system, our observations indicated that unlabeled T-cells exhibited limited movement, while IONPs-labeled T-cells were attracted by magnetic forces towards the magnet with a magnetophoretic mobility of about 2 µm/s, as visually

exemplified in the accompanying movie (**Movie S2)** and quantified in **Figure 2B**. In contrast, non-labeled T-cells and IONPs-labeled T-cells without magnet only show random motion with less than 0.4 μm/s velocity. The attraction of IONPs-labeled T-cells towards the magnet was also visualized with high resolution MRI within agarose gels (**Figure 2C**). Altogether our simple and rapid intracellular labeling procedure for T-cells with citrate-coated IONPs confer both MRI detectability and magnetophoretic mobility without affecting the cell metabolic activity.

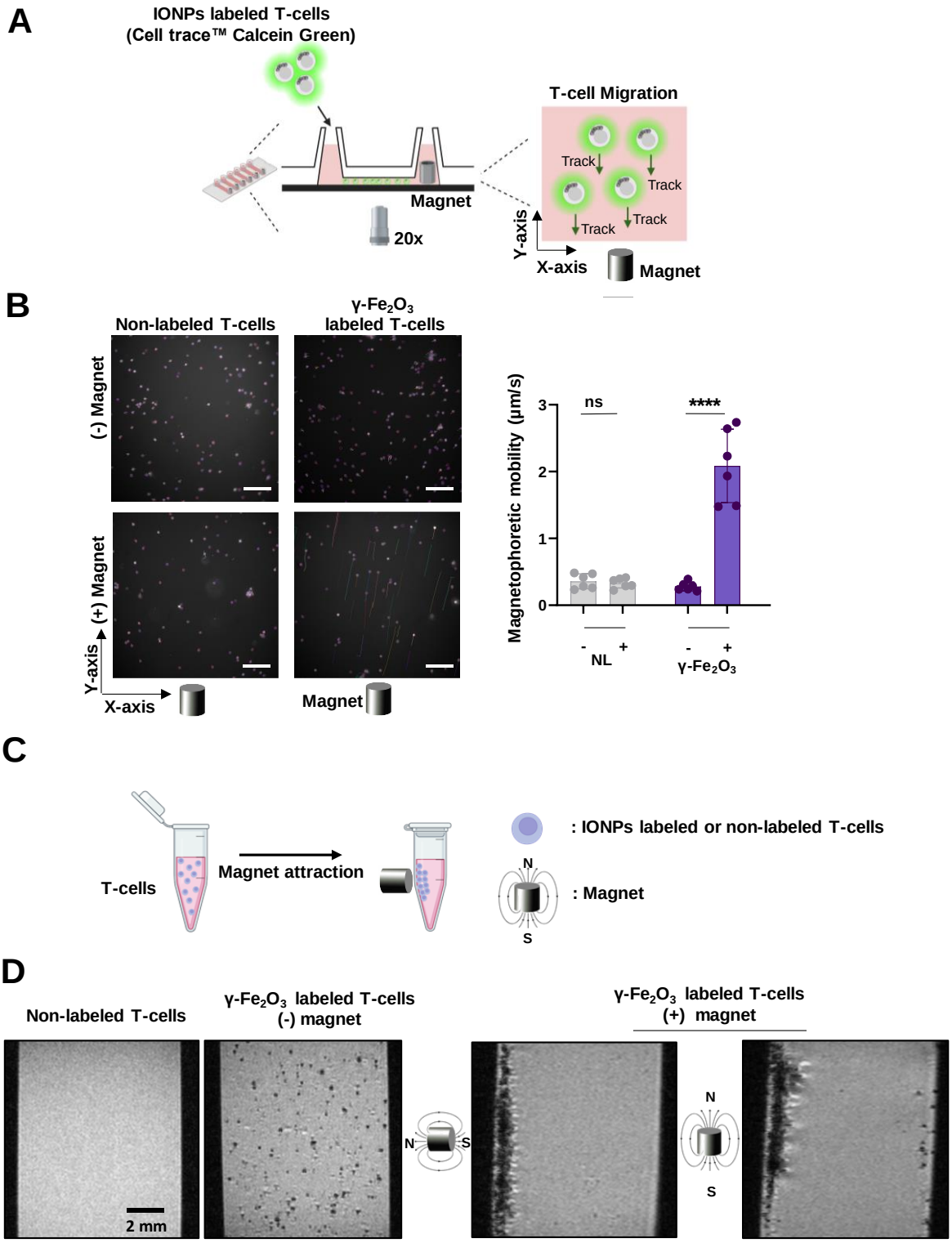

Figure 2. A) Illustration of T-cell attraction toward a magnet in the cell culture medium. Previously activated T-cells were labeled with γ-Fe_2O_3 IONPs (50 µg/mL) for 2 hours and stained with CellTrace™ Calcein Green. T-cells were plated on a 6-channel IBIDI µ-Slide in RPMI medium. Images were acquired using an inverted microscope when the magnet is added.

Time interval: 3 sec; Number of time points: 20. B) IONPs labeled and non-labeled T-cell tracks are shown. Quantification is represented by the measurement of T-cell magnetophoretic mobility (μm/s). The scale bar is 100 μm. C) Schematic illustration of IONPs-labeled T-cell magnet attraction in 0.3% agarose gel. D) Representative high-resolution MRI scans of agarose gels containing 10000 γ-Fe_2O_3 labeled T-cells (50 μg/mL, 2 h incubation) in presence or absence of the magnet (oriented in two different ways with respect to the tube) during the gel formation. The magnet characteristics are shown in **Figure S6**. Results are representative of N=2 independent experiments, n=2 replicates. ****$p < 0.0001$; ns – not significant (one-way ANOVA).

Intracellular IONPs do not affect T-cell phenotype, activation, proliferation and migratory functions

A crucial requirement for the magnetic labeling of T-cells developed in this study is to maintain the T-cell phenotype, proliferation and migratory functions critical for T-cell based immunotherapy. T-cells play a vital role in our immune system, acting as the body's defenders against abnormal cells like tumoral cells.[49,50] Activation is the process that initiates T-cell response, proliferation, and differentiation when they encounter specific threats.[51] Naïve T-cells are in a resting state when they have not been activated by exposure to an antigen. Activation involves a robust and coordinated transition from a quiescent state to an activated, effector state, characterized by enhanced cytokine production, cell proliferation and targeted cytotoxicity.[52,53] CD4 T-cells provide essential signals for immune activation and differentiation, while CD8 T-cells directly engage and eliminate infected or abnormal cells, contributing to the body's defense against infections and cancers. Naïve CD4 and CD8 T-cells, characterized by surface expression of CD62L and CD45RA, encounter for the first time a cognate antigen, which induces their activation. Naïve T-cells then proliferate, acquire a memory phenotype (CD45RA-) and express

early (CD69) and middle (CD25) activation markers. CD62L marker is also used to discriminate between central (CM, CD62L+ CD45RA-) and effector (EM, CD62L- CD45RA-) memory populations, which play a complementary role in the immune response. The expression of these different markers will enable CD4 and CD8 T-cells to perform their proinflammatory function and induce an effective immune response.[54,55] We first analyzed if the stimulated proliferation of different phenotype subsets of T lymphocytes could be affected by IONP labeling. T-cells were labeled with 50 µg/mL IONPs for 2 h and stained with Cell Trace™ Violet (CTV) at Day 0. Then T-cells were stimulated (or not) via CD3 and CD28 (T-cell TransAct™) in presence of IL7 and IL15 cytokines (10 ng/mL) to induce T-cell proliferation. The proliferation of CD4 and CD8 T-cell subsets was analysed by flow cytometry by measuring the dilution of CTV at various time points (Day 2, 5 and 7) post-stimulation, starting from Day 0. Representative CTV fluorescence histograms of IONPs labeled CD4 and CD8 T-cell at day 2, 5 and 7 after stimulation show similar proliferation rate (99% of proliferating cells at day 7) compared to unlabeled stimulated cells (**Figures 3A**). Meanwhile, the non-stimulated cells did not proliferate. We next compared the cell phenotype at day 2, 5 and 7 after stimulation (**Figures S7, S8,** and **S9**). As expected, the percentage of naive T-cells (CD62L+ CD45RA+) is reduced for the stimulated conditions, compared with unstimulated cells. We also found no difference in CD4 and CD8 T-cell ratio and phenotype at day 5 and 7 for activated cells, labeled or not with IONPs (**Figures S7-9**). We observed an increase in the expression of the activation markers CD25 and CD69 after stimulation, compared to unstimulated cells. No difference was noticed except on day 7, when T-cells labeled with IONPs showed prolonged activation, as evidenced by a slight increase in CD25 expression compared to untreated T-cells (**Figure S9**). Overall, our data confirm that IONPs do not interfere with the T-cell activation *in vitro* since proliferation rate and phenotype were not affected.

T-cell migration is another crucial aspect of the immune system's ability to surveil, recognize,

and respond to threats within the body in a regulated way, which involves the orchestrated movement of T-cells throughout various anatomical locations through chemotaxis and active guidance.[56,57] To effectively play their role in immune surveillance, lymphocytes need to respond to chemotactic factors that allow them to enter and exit specific lymphatic organs and tissues. One of the most important chemokine receptors for T-cells is CXCR4 that binds to CXCL12 secreted by lymphoid tissues to mediate T-cell chemoattraction in response to CXCL12 chemokine gradient.[58] To check the potential effect of IONP labeling on T-cell chemotaxis, we first measured the responsiveness of IONP-labeled CEM T-cell line to a CXCL12 chemokine gradient using a Transwell assay (**Figure S10**). Notably, the T-cell line exhibited a migratory response towards the lower chamber, indicative of chemotaxis, and the labeling with IONPs did not significantly affect their migration compared to the control. Furthermore, we used video microscopy to quantitatively analyze the dynamic migratory behavior of primary UNT T-cells in 3D collagen gel mimicking the tumor extracellular matrix (ECM). To distinguish the migration of non-labeled T-cells and IONP-labeled T-cells, these cells were stained with CellTrace™ Calcein Red and CellTrace™ Calcein Green, respectively, plated on μ-Slide in collagen gel and their displacements were tracked (**Figure 3B**). Unlabeled and IONP-labeled T-cells both migrated in the collagen gel and there was no significant difference in both the percentage of migrating cells (Non-labeled: 64±9%, IONP-labeled: 57±9%) and in their mean displacement speed (Non-labeled: 5.5±0.4, IONP-labeled: 5.3±0.6 μm/min) (**Figure 3C** and **supplementary Video S1**). Altogether, our conditions of T-cell magnetic labeling did not affect cellular chemotaxis and migration capacity in ECM mimicking collagen scaffold.

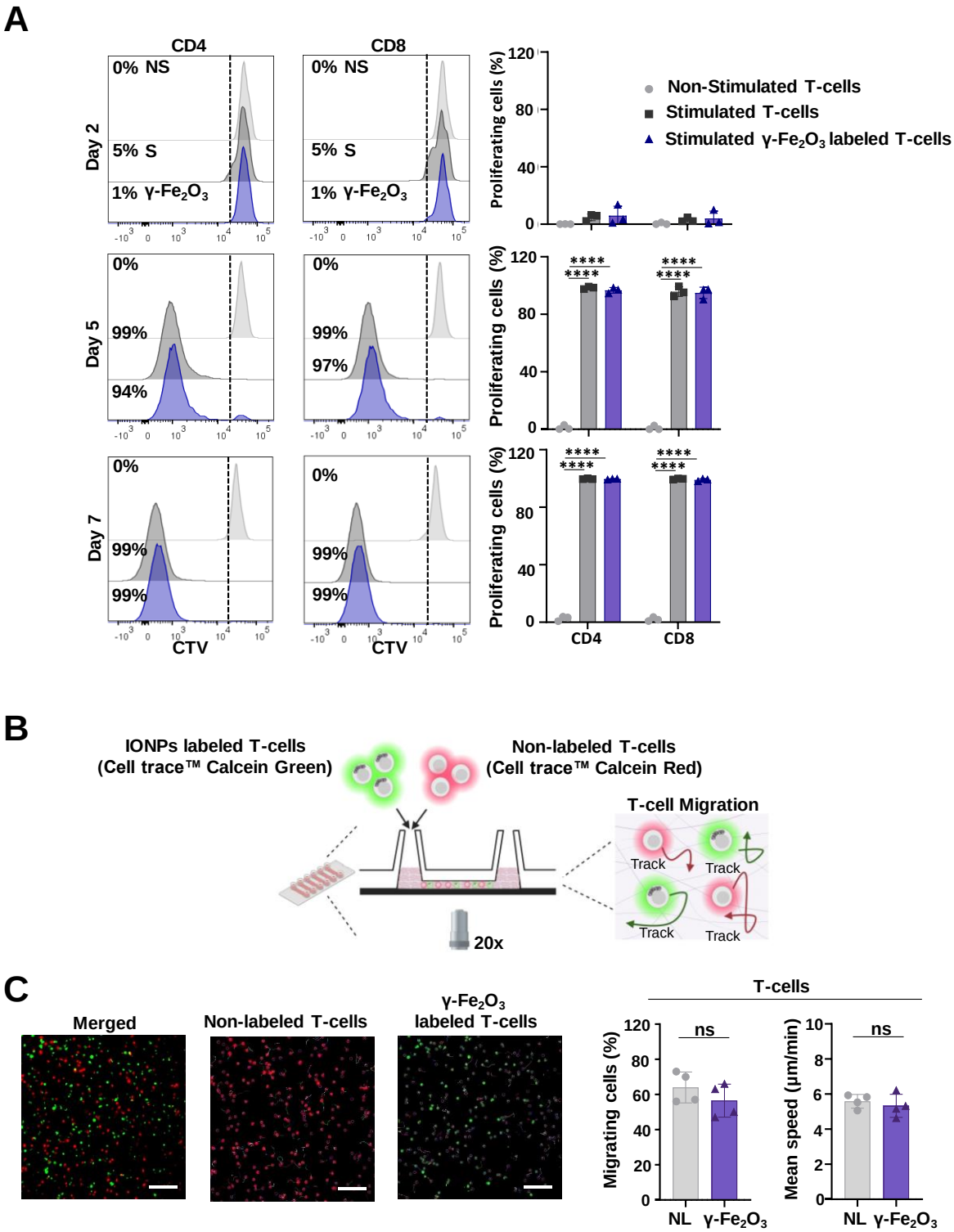

Figure 3. A) T-cells were stimulated by anti-CD3 and CD28 coated beads (T-cell TransAct™), IL7 and IL15 cytokines (10ng/mL). T-cells were labeled with γ-Fe_2O_3 IONPs (50 µg/mL) for 2 hours and stained with Cell Trace™ Violet at Day 0. At different time points (Day 2, 5 and 7) proliferation of CD4 and CD8 positive T-cells was assessed by flow cytometry. Representative

histograms of proliferating γ-Fe_2O_3 IONPs (purple) labeled T-cell at day 2, 5 and 7 are shown. Non-stimulated and non-labeled T-cells (NS) represent the negative control (Light grey). Stimulated and non-labeled T-cells (S) are the positive control (Dark grey). Percentage of CD4 and CD8 positive proliferating cells was quantified in each group (right) (n=3 independent experiments). B) Scheme of T-cell migration experiment. T-cell were stimulated, labeled with γ-Fe_2O_3 IONPs and stained with CellTrace™ Calcein Green. Non-labeled stimulated T-cells were stained with CellTrace™ Calcein Red. T-cells were plated on a 6 channel IBIDI μ-Slide in 2mg/mL of collagen gel and tracked. Time interval: 30 sec; Number of time points: 15. C) Tracks of merged T-cells (left), non-labeled T-cells (middle) and γ-Fe_2O_3 IONP (right) labeled T-cells are represented. Percentage and mean speed of migrating cells are quantified for non-labeled T-cells (NL, grey) and γ-Fe_2O_3 IONP (purple) labeled T-cells, showing no significant difference (n=4). The scale bar is 100 μm. ****$p < 0.0001$; ns – not significant (unpaired 2-tailed t-test or one-way ANOVA with a Tukey's multiple comparison test).

Intracellular IONPs do not affect CAR expression, specificity and cytotoxicity of EGFR CAR T-cells against EGFR-expressing A549 tumor spheroids

EGFR is the epidermal growth factor receptor inducing intrinsic tyrosine kinase function.[59] EGFR mutations are associated with various types of tumors, notably lung and breast cancer, representing a relevant immunotherapeutic target.[60] Here, to study the activity of EGFR CAR T-cells, we used the tumor cell line A549 isolated from human lung adenocarcinoma and expressing EGFR on the cell surface. EGFR CAR T-cells should therefore recognize the target on the cell line and undergo activation. A mandatory prerequisite was to check whether the IONP labeling could maintain the CAR T-cell specificity to recognize the EGFR target. To this end, we initially assessed the CAR expression by measuring the percentage of EGFP and performing anti-EGFR CAR staining on transduced and non-transduced T cells, with or without

IONP labeling, using flow cytometry. Figure S3 shows that both the GFP expression and CAR expression are not significantly modified in the transduced CAR T-cells after labeling with IONP (50 μg/mL, 2h) reaching about 60 % of the cells similarly to non-labeled CAR T-cells. GFP and EGFR CAR were not expressed in UNT labeled and non-labeled T-cells. These results thus confirm that IONPs do not interfere with the CAR expression on the cell membrane, owing to their independent non-specific internalization pathway. Subsequently, we investigated the activation of EGFR CAR T-cells against the EGFR-expressing A549 cell line by analyzing calcium response and cytokine secretion, which reflects CAR-dependent T-cell activation. Indeed, when CAR T-cells encounter their targets, CAR engagement triggers intracellular signals including an increase in intracellular calcium.[61] After several hours, activated CAR T-cells produce various pro-inflammatory cytokines (INF-γ, TNF-α...).[62,63]

To monitor their intracellular calcium concentration, EGFR CAR and UNT T-cells were first loaded with the cell permeant Fura-2 cytosolic Ca^{2+} dye and then added on a monolayer of A549 cells (**Figure 4A**). Micrographs in **Figure 4A** show that the UNT T-cells produced a weak calcium response, while EGFR CAR-T-cells demonstrated a strong intracellular calcium increase. Quantification of the fluorescent signal shows a higher calcium peak for CAR T-cells compared with UNT T-cells (**Figure 4A**). Regarding the secretion of pro-inflammatory cytokines, EGFR CAR T-cells significantly produced higher concentrations of IFN-γ (Ratio CAR T-cells/UNT T-cells: 255±135), Granzyme B (93±116), TNF-α (42±26), Perforin (4±3) and sFasL (7±3.7) in comparison to UNT T-cells after 24 h of co-culture with A549 cells (**Figure 4B** and **Figure S11**). These experiments also enabled us to verify that IONPs had no impact on the activation and specificity of EGFR CAR-T-cells against the A549 cell line. Indeed, there was no difference between IONP-labeled and non-labeled CAR T-cells in term of calcium response and cytokine secretion (**Figure 4A** and **4B, Figure S11**). Similarly, IONP-labeled and non-labeled UNT T-cells behaved in the same manner.

We further tested the efficacy and specificity of EGFR CAR T-cells against spheroids formed from EGFR-expressing A549 cells (**Figure 4C)**. Such spheroids are considered as an *in vitro* model of solid tumors and might be less prone to CAR T-attack compared to 2D-culture due to 3D organization. The A549 spheroid formation occurred over a period of 4 days (**Figure S12**), in a low attachment 96-well plate, followed by a co-culture with CAR T-cells or UNT T-cells for additional 5 days (day 0 to day 5 in **Figure 4C**). We observed that the relative size of control spheroids non-exposed to T-cells remained constant throughout the five-day experiment due to contact inhibition in 3D, as described by others.[64] Conversely, the size of spheroids initially increased in the presence of either UNT T-cells or CAR T-cells during the first two days (by 50 and 25 %, respectively). The spheroid size then returned to control levels for UNT T-cells and dropped by 50% below control levels for CAR T-cells. This process was accompanied by a visible dismantling of the spheroid, characterized by a loose rim composed of dead cells around the spheroid core (**Figure 4C**). Thus, compared to control spheroids and spheroids exposed to UNT T-cells, EGFR CAR T-cells induced a significant reduction in tumor spheroid size over the 5-day period following the initiation of the CAR T-cell attack assay. The specificity and potency of CAR T-cells in spheroid destruction was further supported by **Figure 4C** showing the ability of CAR T-cells to infiltrate the A549 tumor spheroid, while UNT T-cells remained localized at the periphery of the structure. Importantly the same assay was performed with IONP-labeled CAR T-cells and UNT T-cells showing no difference with the non-labeled T cells and no compromise in EGFR directed CAR T-cell cytotoxicity against tumors. This spheroid test was shown to be a robust and high-throughput functional assay for simultaneous testing of different conditions of CAR T-cell activity, demonstrating that magnetic labeling with γFe_2O_3 IONPs remarkably preserved the specific cytotoxicity and tumor infiltration of EGFR CAR T-cells in comparison to the untransduced T-cells. To further refine the tumor model and mimic multicellular TME with enhanced compactness and rigidity, we incorporated fibroblasts with

the tumor cells (ratio of 1:4) for the tumor spheroids formation (**Figure S13**). We thus monitored for 7 days the effect of UNT T-cells and IONP-labeled or non-labeled CAR T-cell on multicellular spheroids. Akin to previous observations, we noted a slight increase in tumor spheroid volume attributed to EGFR CAR T-cell infiltration at the initial stages of the assay. Subsequently, EGFR CAR T-cells, labeled or non-labeled with IONPs, effectively exerted cytotoxicity, leading to a rapid reduction in tumor spheroid volume. This underscores the potent and specific cytolytic activity of EGFR CAR T-cell compared to UNT T-cell in multicellular tumoroids, unaffected by IONP labeling. Given the demonstrated total innocuousness of our IONP labeling on (CAR) T-cell proliferation, activation and EGFR-specific antitumor potency *in vitro*, the next step was to exploit their MRI detectability for longitudinal monitoring of CAR T-cell immunotherapy in mice.

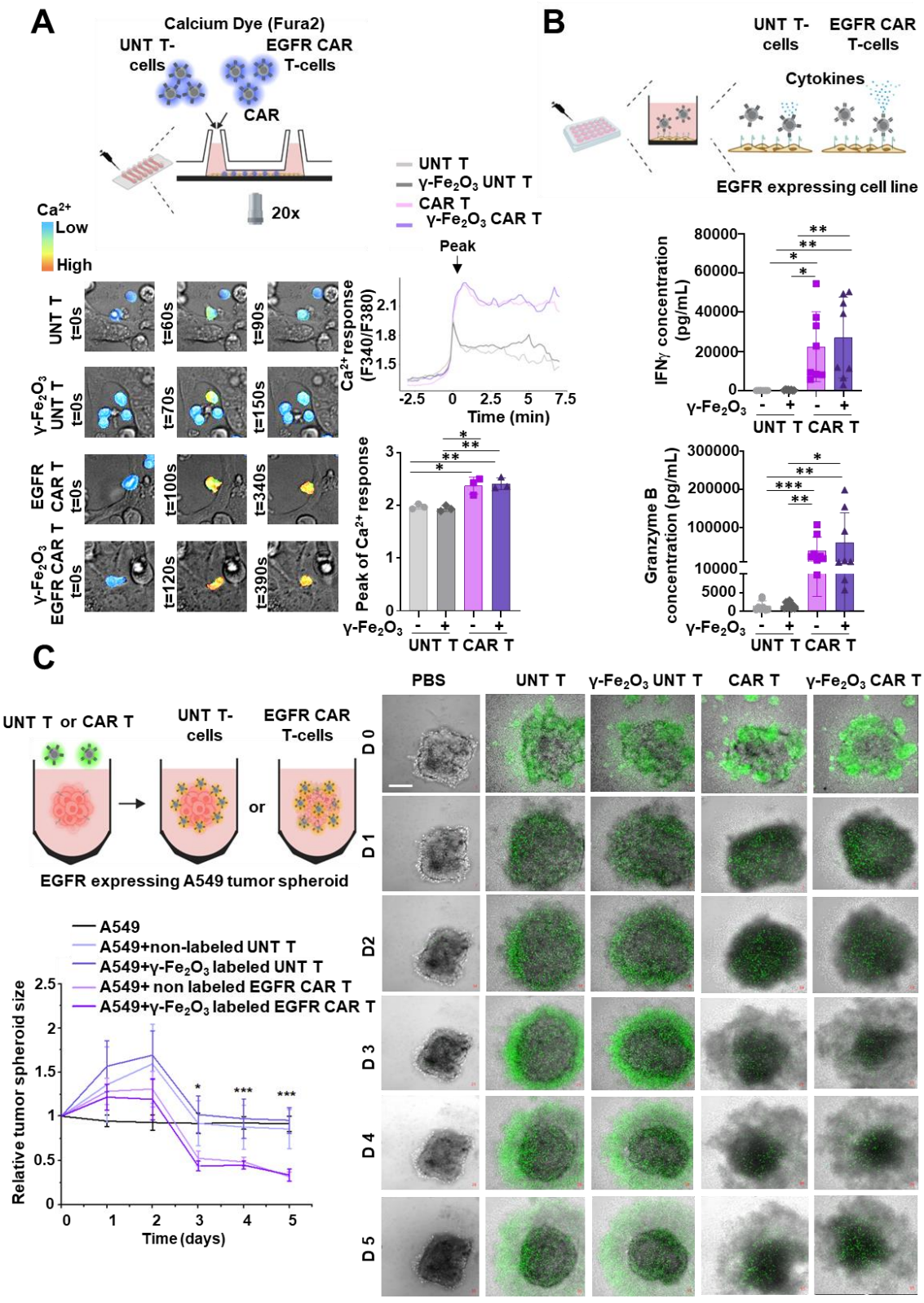

Figure 4. A) Ca^{2+} responses of EGFR CAR T-cells during their contact with A549 tumor cells. Illustration summarizing the calcium and cytokine assay (top). γ-Fe_2O_3 IONP-labeled or non-labeled UNT T-cells and CAR T-cells were loaded with $Fura2^{AM}$ and added to A549 cells pre-

plated in a 6-channel IBIDI μ-Slide. Images were acquired every 10 sec during 10 min at 350 and 380 nm excitation wavelength using Meta Fluor software. Representative micrographs of a calcium-responsive cell for each condition are shown (bottom). The F340/F380 ratio curves indicative of the average calcium responses are presented (bottom right). The peak of F340/F380 ratio in the calcium response curve is quantified (bottom right) (n=4). B) CAR T-cell production of cytokines during their contact with A549 tumor cells. γ-Fe_2O_3-labeled or non-labeled UNT T-cells and CAR T-cells were added to A549 cells pre-plated in a 48-well plate. After 24 hours of coculture, supernatants were collected and cytokines measured using LEGENDplex™ kit (right). Quantification of IFN-γ and Granzyme B concentration (pg/mL) are presented (bottom) (n=4; duplicate). C) CAR T-cell attack assay on A549 tumor cell spheroids. The experimental set up (top left): after their formation in 96-well cell anti adherent plate for 4 days (**see Figure S12**), the tumor spheroids were either exposed to γ-Fe_2O_3 IONP-labeled or non-labeled UNT T-cells and CAR T-cells, stained with CellTrace™ Calcein Green, for 5 consecutive days (Day 0 to Day 5). Within next 5 days the size of spheroids was followed in a time-lapse acquisition in two channels: green epi-fluorescence for CellTrace™ Calcein Green and bright field for spheroid shape. Changes in the relative size of the spheroids, normalized to D0, were quantified throughout the duration of the experiment. Scale bar is 200 μm. Results are representative of one experiment performed in triplicate and values are presented as mean ±SD. *$p<0.05$, **$p<0.01$, ***$p<0.001$ (One-way ANOVA).

In vivo longitudinal MRI monitoring of CAR T-cell immunotherapy over fourteen days reveals earlier and enhanced tumor infiltration of EGFR CAR T-cells in comparison to non-transduced T-cells

To monitor T-cell trafficking and antitumor efficiency of EGFR CAR T-cell in preclinical solid tumor model, three groups of mice bearing A549 subcutaneous xenograft were compared,

injected intravenously at day 0 with 1 million of non-labeled EGFR CAR T-cells (n=3), of γ-Fe_2O_3 IONP-labeled EGFR CAR T-cells (n=2) and of γ-Fe_2O_3 IONP-labeled UNT T-cells (n=3) (**Figure 5A**). Following cell injection, the body weight and tumor growth were monitored (**Figure 5B**). There was no difference in the weight of the mice in each group. However significant tumor growth stabilization was observed after approximately 2 weeks following administration of EGFR CAR T-cells, labeled or not with IONPs, compared to the non-transduced IONP-labeled UNT T-cells. These results first confirmed the specificity of EGFR CAR T-cells to induce tumor growth arrest in this EGFR-expressing A549 lung tumor model in comparison with the UNT T-cells. Second, it shows that IONPs did not affect the antitumor therapeutic ability and specificity of EGFR CAR T-cells in comparison to the untransduced T-cells *in vivo*, confirming our extensive *in vitro* functional study reported above.

In parallel, for longitudinal monitoring of CAR T-cell distribution *in vivo*, we performed two different MRI imaging protocols at consecutive time points over 14 days following systemic injection of T-cells : 1) high-resolution T2*-weighted MR imaging (HR MRI) of the tumor *in vivo* to compare the tumor infiltration and efficacy of EGFR CAR T-cells and UNT T-cells, and 2) whole-body MR imaging (WB MRI) of mice to monitor the distribution of T cells within various organs at different time points. Before T-cell administration (day 0), HR MRI of the tumor showed similar aspects in the 3 groups with homogeneous signal and eventually a few signal voids, as shown in **Figure 5C**. However, from 7 days after T-cell injection, the heterogeneity of the tumor signal intensified in the three groups, with greater intensity observed in the γ-Fe_2O_3-labeled EGFR CAR T-cells group compared to both the γ-Fe_2O_3-labeled UNT T-cells and to non-labeled EGFR CAR T (**Figure 5C)**. We observed the coexistence of large hypointense areas that extended over multiple successive MR scan slices and of much smaller dispersed punctuated signal voids (dot-like structures in all of the three projection planes) resembling the signal voids observed in the agarose gels that contained dispersed γ-Fe_2O_3-

labelled T-cells (**Figure 1E**). To quantitatively evaluate the spatial extension of hypointense zones, image analysis was performed on sagittal sections of the whole tumor scan at each time point after cell administration. [65] Video compiling successive MRI scans for all mice and time-points are available in supporting materials (**Video S3**). Each dark area was depicted over the successive MR sections of the tumor and the number of voxels it contained was quantified. [65] The 3D signal voids were categorized in two categories: the punctuated dots with less than 100 voxels, likely corresponding to the scattered IONP-labeled cells, and the larger signal voids with more than 100 voxels, probably related to large conglomerates of IONP-labeled cells and/or necrotic areas (see **Figure 5D**, and **Figure S14** for the longitudinal analysis of hypointense zones in each individual tumor). Among the inducers of signal losses, it was not possible with this set up to differentiate between the necrosis zone caused by cytotoxic CAR T-cells - whether IONP-labeled (thus further reducing the signal) or unlabeled - and the infiltration of labeled-T cells into the tumor. Of note the extended dark areas were located preferentially at the core of the tumor and probably superimposed with the presence of cytotoxic effector T-cells. Interestingly, the total volume of the tumor devoid of MR signal was increasing over time in the three groups, probably due to the increasing extension of necrosis (**Figure 5D left**). However, the total hypointense volume was larger in the group injected with IONP-labeled EGFR CAR T-cells at day 7 and even significantly larger at day 10 in comparison to non-labeled EGFR CAR T-cells and to IONP-labeled UNT T-cells. These results suggest that EGFR CAR T-cells were more rapid and more efficient to infiltrate the tumor and to induce necrosis than their non-transduced counterparts. Under conditions involving IONPs, the signal loss within the tumor is likely attributed to both the infiltration of IONP-labeled CAR T-cells and necrosis resulting from tumor cell death. Conversely, in the case of non-labeled CAR T-cells, the signal loss is primarily due to necrosis. We also quantified the total volume of punctuated dots with less than 100 voxels (**Figure 5D right**) and the volume of the large hypointense zones with

more than 100 voxels (**Figure 5D middle**). The scattered punctuated signal voids (<100 voxels) represented about 10% of the total hypointense volume and were increasing until day 10, more predominantly in the group injected with IONP-labeled CART T-cells, suggesting that they could reflect T-cell infiltration in the tumor. At the latter time point, all the labeled T- cells could colocalize with necrosis zones, thus reducing the signal loss extension in comparison to day 10. Interestingly, the maximum of MR hypointense tumor volume was found at the same time point from which the arrest of tumor growth was observed in the groups treated with EGFR CAR T-cells (**Figure 5B**) compared to UNT T-cells. Overall, the increase of hypointense volumes and their distribution in the tumor can be used as a proxy to monitor the antitumor efficacy of the T-cell therapy, being more efficient with EGFR-directed CAR T-cells in comparison to primary UNT T-cells.

Apart from high resolution MRI of tumors, whole-body MRI at the different time points allowed MR signal quantification in key organs (liver, tumor, and kidney, **Figures S15 and S16**) and particularly in the spleen (**Figure S15**), which can be infiltrated with T cells. In WB MRI, the spleen can be visualized as part of the abdominal imaging protocol. The spleen plays a crucial role in supporting T-cell function. It serves as a vital organ for T-cell activation, involves antigen presentation, T-cell receptor recognition, co-stimulation, clonal expansion, and migration for targeted immune response.[66,67] From day 1 post-administration and at all further time points, the MR signal in the spleen was smaller in the γ-Fe_2O_3-labeled EGFR CAR T-cell group in comparison to the γ-Fe_2O_3-labeled UNT T-cell group, which was also smaller in comparison to the non-labeled EGFR CAR T-cell group (**Figure S15A**). This suggests first that T-cells (both EGFR CAR T-cell and UNT T-cell) were homing to the spleen since their IONP labeling induced signal intensity loss in the spleen. Secondly, this indicates that EGFR CAR T-cells and UNT T-cells exhibit a distinct pace of spleen recruitment and activation. At day 1, both labeled UNT and CAR T-cells induced a similar signal loss in the spleen, indicating early

and non-specific recruitment of both T-cell populations. However, at later time points, the signal in the from the IONP-labeled UNT T-cell group increased up to the basal level of the non-labeled EGFR CAR T-cell group, suggesting clearance of non-transduced T-cells from the spleen. In contrast, IONP-labeled EGFR CAR T-cells, due to corresponding antigen stimulation, were activated and could eventually proliferate in the spleen, maintaining signal loss in this organ. This result was corroborated by the flow cytometry analysis of the spleen on day 14, which reveals a higher percentage of CAR T-cells compared to the UNT T-cell. The CD3+ cell percentage in the UNT T-cell condition was similar to that in control mice injected with PBS, indicative of the background staining **(Figure S15B**). In parallel, we found no differences in the MRI signal of the liver and kidney of the 3 different groups (**Figure S16**) over the follow-up from day 1 to day 9. This strongly supports the hypothesis that IONPs were still associated with the T-cells over the 10 days. If T-cells would be lysed and/or if they would release their magnetic cargo, or if T-cells and/or their load would be engulfed by macrophages, the nanoparticles would accumulate in the liver or could be eliminated by the kidney, as it is usually observed after intravenous administration of IONPs.[68,69] This would result in hypointense signals in the liver and/or kidneys, respectively, which was clearly not the case in our study.

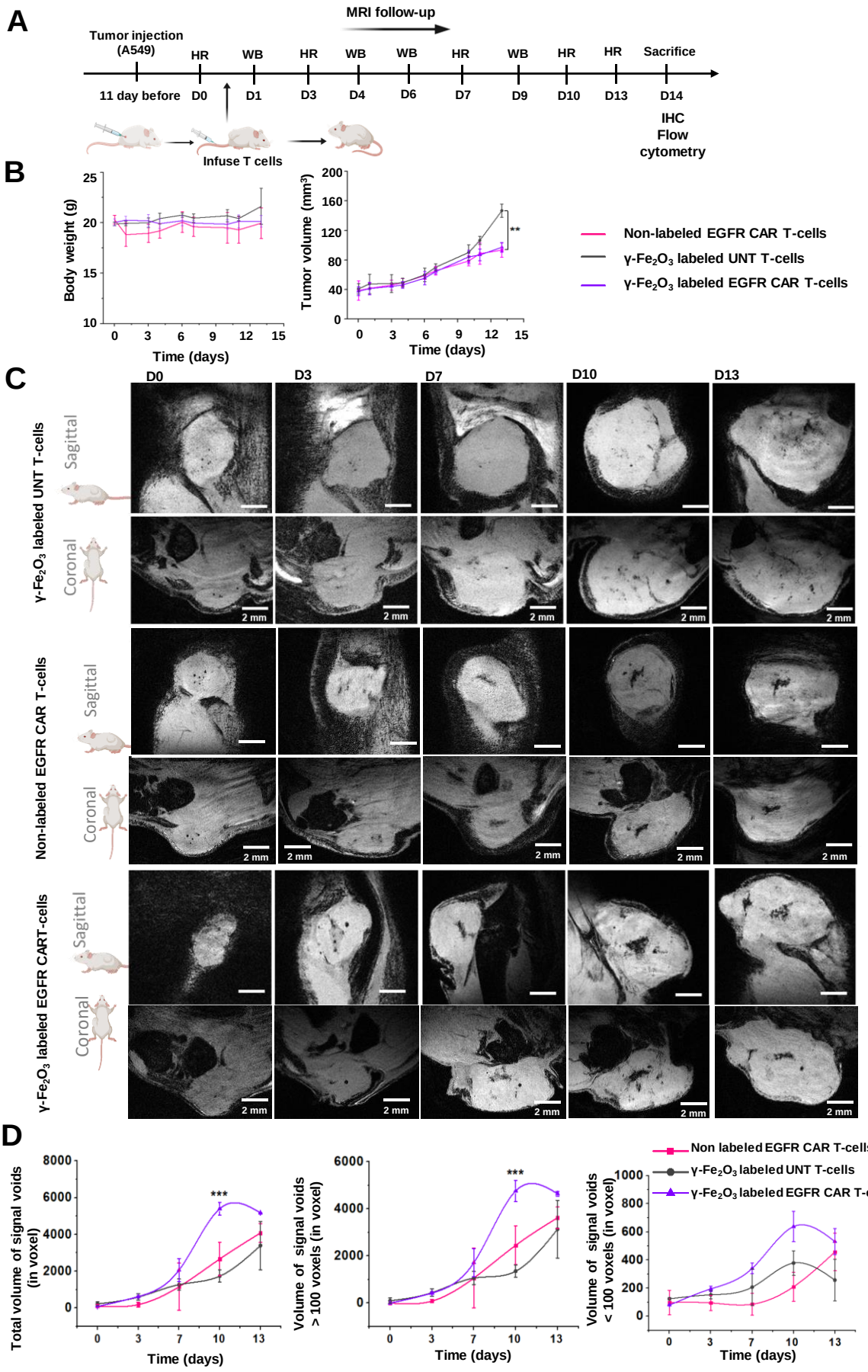
A
MRI follow-up
Tumor injection (A549)
HR
WB
HR
WB
WB
HR
WB
HR
HR
Sacrifice
11 day before
D0
D1
D3
D4
D6
D7
D9
D10
D13
D14
Infuse T cells
IHC
Flow cytometry
B
Body weight (g)
Time (days)
Tumor volume (mm³)
Time (days)
**
Non-labeled EGFR CAR T-cells
γ-Fe2O3 labeled UNT T-cells
γ-Fe2O3 labeled EGFR CAR T-cells
C
D0
D3
D7
D10
D13
γ-Fe2O3 labeled UNT T-cells
Non-labeled EGFR CAR T-cells
γ-Fe2O3 labeled EGFR CART-cells
Sagittal
Coronal
2 mm
D
Total volume of signal voids (in voxel)
Volume of signal voids > 100 voxels (in voxel)
Volume of signal voids < 100 voxels (in voxel)
***
Time (days)
Non labeled EGFR CAR T-cells
γ-Fe2O3 labeled UNT T-cells
γ-Fe2O3 labeled EGFR CAR T-cells

Figure 5. A) Schematic representation of the MRI procedures applied in the animal experiment protocol and representative MR scans of the whole body (WB) and tumor high resolution (HR) MRI follow up. B) Mice body weight increase over time and tumor growth over time in different groups. C) Representative longitudinal high resolution tumor monitoring obtained from MR scans, presented as minimum intensity projections of a 500 µm thick volume of sagittal or coronal sections, at day 0 (pre-administration of T-cell), day 3, day 7, day 10 and day 13. Scale bar corresponds to 2 mm. D) Quantification of the total volume (in number of voxel) of signal voids averaged for the different mice of each group at the different time points (left), of the volume of signal voids with more than 100 voxels (middle), and of the volume of signal voids with less than 100 voxels (right). N=3 mice per group; values are presented as mean ± SD. **p<0.01, ***p<0.001 (One-way ANOVA).

To confirm the preferential tumor infiltration of EGFR CAR T-cells in comparison to UNT T-cells suggested by MRI longitudinal follow-up, tumors were analyzed *ex vivo* at day 14, the latest time-points of the follow-up. Anti-CD3 immunohistology was used to localize the accumulation of γ-Fe_2O_3 IONP-labeled or non-labeled EGFR CAR T-cells and UNT T-cells within the tumor (**Figure 6A** top panel) and Prussian blue staining was used to localize IONPs (**Figure 6B** bottom panel). Mice injected with non-labeled EGFR CAR T-cells showed widespread distribution of CD3+ T-cells, which were not revealed by Prussian blue staining (as they did not contain iron). γ-Fe_2O_3-labeled UNT T-cell group was characterized by only sparsely distributed CD3+ T-cells and low Prussian blue staining in tumors. In contrast, in the group injected with γ-Fe_2O_3-labeled EGFR CAR T-cell, blue-stained zones were associated with infiltration of CD3+ T-cells in tumors. Therefore, *ex vivo* CD3+ T-cell localization associated with Prussian blue corroborates *in vivo* HR MRI in tumor sites, confirming larger infiltration of EGFR CAR T-cell in comparison to UNT T-cell. Meanwhile, Prussian blue

staining of other vital organs, including the heart, kidney, lung, and liver, across the three experimental groups revealed no discernible distinctions (**Figure S17**). Moreover, flow cytometry results confirmed the stronger infiltration of CAR T-cells compared to UNT T-cells in the tumor, with higher percentage of CD3+ T-cells (**Figure 6**) after CAR T-cell administration. There was also no difference in the percentage of CD3+ T-cells between γ-Fe_2O_3-labeled and non-labeled EGFR CAR T-cells groups. As expected, no positive CD3 cell labeling was observed in the condition injected with PBS alone (**Figure 6B**). Finally, the H&E staining of murine organs (heart, liver, spleen, lung, and kidney) show no abnormality and no difference in the 3 different groups, suggesting that the injection of EGFR CAR T-cells and UNT T, labeled or not-labeled with IONPs was not hazardous to mice's vital organs (**Figure S18**).

To sum up, we demonstrated that our innocuous protocol for intracellular labeling of T cells with IONPs offers unique opportunity to monitor longitudinally and in a non-invasive manner the CAR T-cell immunotherapy in preclinical lung tumor model up to 14 days after cell administration. MRI monitoring provides valuable kinetic information on the fate, biodistribution of T cells and antitumor effect, showing distinct pace of splenic distribution and tumor infiltration of EGFR-directed CAR T-cell in comparison to untransduced T cells, and correlating with antitumor efficiency of CAR T-cell against EGFR expressing tumor. Importantly, *in vivo* MRI follow up of the therapeutic regimen correlated well with *ex vivo* immunohistological results at the latest time points of the protocol. As IONP-labeled CAR T-cells are as efficient as their non-labeled counterparts to specifically attack the EGFR expressing tumors, while allowing MRI monitoring of T cells, this clinically-compatible approach could be of considerable interest to follow up the outcome of CAR T therapy in solid tumors in clinical practice.

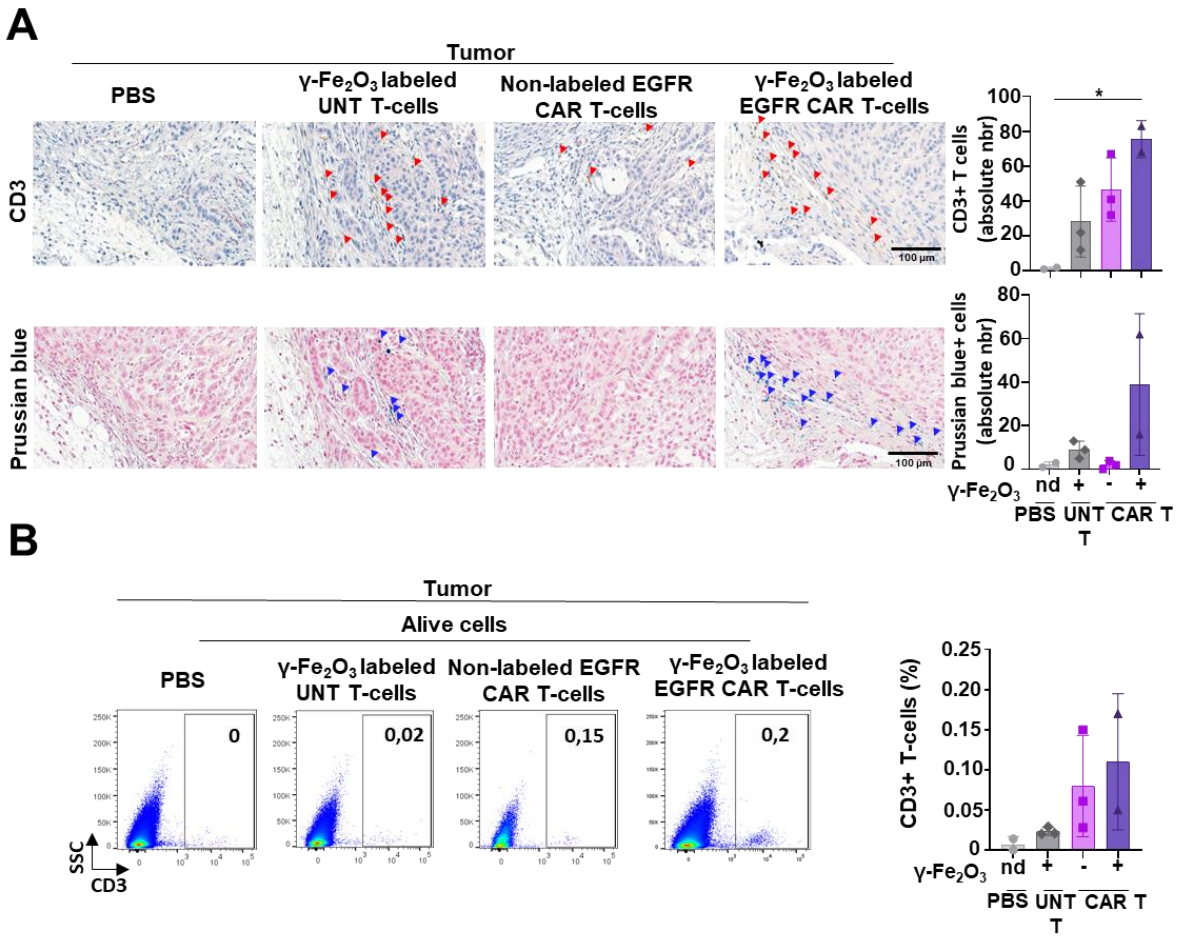

Figure 6. A) Representative histology of CD3 and Prussian blue of tumor sections obtained after mice sacrifice. Mice were intravenously injected with γ-Fe_2O_3 IONP-labeled and non-labeled UNT T-cells and EGFR CAR T-cells and sacrificed at day 14. The brown coloration corresponds to the presence of positively stained CD3 cells (red arrows), while the blue coloration corresponds to the presence of iron oxide nanoparticles (IONPs) (blue arrows). The scale bar is standardized at 100 µm. N=3 mice per group; values of n=3 images per animal are presented as mean ±SD. *$p < 0.05$ (One-way ANOVA). B) Flow cytometry for expression of CD3 in cells dissociated from the tumors. Quantification of the percentage of these subsets is shown. N=3 mice per group.

Magnetic attraction potentiates the early homing of IONP-labeled EGFR CAR-T cells to the tumor and enhances the CAR T antitumor effects

Solid tumors impede T-cells from effectively combating cancer through mechanisms such as immune evasion, a hostile tumor microenvironment that limit T-cell penetration, and antigenic variations that jeopardize tumor cells recognition and T-cell chemotaxis.[70] In order to improve T-cell homing, we tested a physical strategy, independent of biochemical and environmental cues, to enhance the tumor accumulation of T-cells by taking advantage of the magnetophoretic mobility of IONPs-labeled T-cells. Three groups of mice were compared to assess the effect of an external magnet, positioned over the tumor zone, to induce a magnetic attraction of IONP-labeled CAR T-cells to the tumor site: a test group bearing a magnet, injected intravenously at day 0 with 1 million γ-Fe_2O_3-labeled EGFR CAR-T-cells (n=3) and two "control" groups, the first one bearing a magnet and injected with non-labeled EGFR CAR T-cells (n=3) and the second one without magnet injected with γ-Fe_2O_3 labeled EGFR CAR-T-cells (n=3). Note that the magnet was temporally retrieved during each HR or WB MRI acquisition and was removed definitively from the mouse between day 4 and day 5 following CAR T-cells injection (**Figure 7A**). To assess the therapeutic efficacy of magnetically guided EGFR CAR T-cell intervention *in vivo*, tumor growth was measured (**Figure 7B**). Remarkably, treatment with IONP-labeled EGFR CAR T-cells in the presence of a magnet resulted in reduced tumor growth compared to the two control groups: one without a magnet and the other with non-labeled EGFR CAR T-cells. This divergence in tumor growth trajectories became evident approximately one-week post-administration (**Figure 7B**, right). Importantly, there were no discernible differences in the weights of the mice across all experimental groups (**Figure 7B**, left), thereby ruling out confounding factors related to systemic effects. We next examined the evolution of the T2*-weighted high-resolution MR imaging of each tumor in the different groups at day 3, day 6, day 9 and day 13 post-injection as exemplified in **Figure 7C**. Video compiling successive MRI scans for all mice and time-points are available in supporting materials (**Video S4**). Importantly the effect of the magnet on the IONP-labeled EGFR CAR T-cells was clearly visible from the

first time point of observation (day 3) in comparison to the non-labeled EGFR CAR T-cells, or to the IONP-labeled EGFR CAR T-cells in absence of magnet. Indeed, we observed very large hypointense regions in the tumor at the first time points in mice bearing the magnet and injected with IONP-labeled EGFR CAR T-cells at day 0 (**Figure 7C**). This distinctive spatial pattern may be ascribed to the attraction of the magnet that favors a localized and early accumulation of the labeled CAR T-cells. In contrast, the groups with non-labeled CAR T-cells with magnet or labeled CAR T-cells without magnet resembled the MR signal pattern of the corresponding groups in the previous experiment of **Figure 5**, with no effect of the magnet. We applied the same method as in **Figure 5** to quantify the hypointense zones in each tumor (see **Figure S19** for the follow up of each individual mouse, or **Figure 7D** for the average volume across the groups). Importantly the total volume of hypointense regions was shown to be enhanced by the magnet, mostly at the shortest time points of observation before one week. In comparison, the volume of hypointense regions started to increase at later time points (from one week after injection) for IONP-labeled EGFR CAR T-cells in absence of magnet, and to a lesser extent for the non-labeled EGFR CAR T-cells. A similar evolution was observed for the volume of punctuate signal voids (<100 voxels) showing enhanced and earlier infiltration of IONP-labeled CAR T cells due to the magnet in comparison to the spontaneous tumor homing of EGFR CAR T-cells. Remarkably such longitudinal non-invasive MRI assessment of the magnetically improved CAR T-cell infiltration in tumors temporally correlates with the outcome on tumor growth curve **(Figure 7B)** which splits at day 7 the magnetic group from the two control groups.

Apart from tumor localization, WB MRI in **Figure S20** suggests that IONP-labeled EGFR CAR T-cell group exhibited splenic homing and residence, when the magnet was not applied, which is consistent with our previous results. Intriguingly, IONP-labeled EGFR CAR T-cell with magnet group did not exhibit spleen localization, with the MR signal pattern resembling that of the non-labeled EGFR CAR T-cell with magnet group (**Figure S20**). Upon removal of

the magnet, there was a discernible, although not significant, augmentation in splenic MR signal intensity within the γ-Fe_2O_3-labeled EGFR CAR T-cell group, indicative of a potential initiation of homing to the spleen (**Figure S20**). The observed alterations in splenic MR signals suggest that the magnet exerts an attractive force, facilitating increased accumulation of IONP-labeled EGFR CAR T-cells within the tumor microenvironment, to the detriment of spontaneous splenic homing at short times. In addition, IHC analysis at day 14 after CAR T-cell injection confirms that γ-Fe_2O_3-labeled EGFR CAR T-cells infiltrated the tumor to a higher extent in presence of the magnet (**Figure 8A**). These findings collectively highlight the pivotal role of magnetic guidance in modulating the trafficking of magnetically-labeled EGFR CAR T-cells both in spleen and tumor microenvironment with clear outcomes on CAR T-cell accumulation and on tumor growth reduction. Meanwhile, during the 8-day WB MRI follow-up, no discernible differences in MR signals were observed in the liver and kidneys among the three groups (**Figure S21**), while the tumor shows a tendency towards lower signal when labeled EGFR CAR T-cells were injected in presence of the magnet. In addition, H&E, Anti-CD3 and Prussian blue staining of heart, kidney, lung, and liver revealed no abnormalities or disparities among the three groups (**Figures S22** to **S24**), confirming that the inclusion of a magnet did not trigger adverse effects in those vital organs.

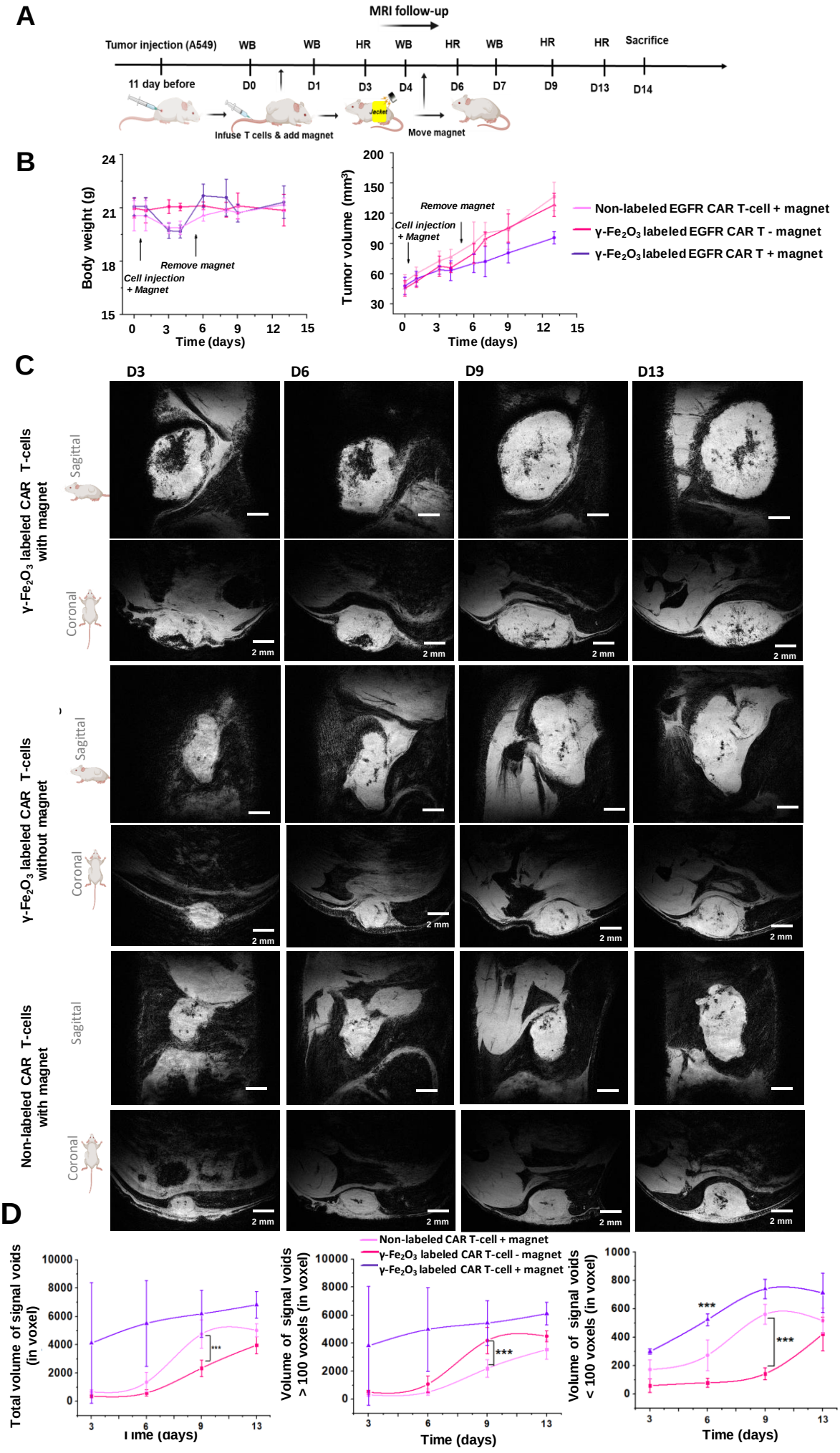
A
MRI follow-up
Tumor injection (A549)
WB
WB
HR
WB
HR
WB
HR
HR
Sacrifice
11 day before
D0
D1
D3
D4
D6
D7
D9
D13
D14
Jacket
Infuse T cells & add magnet
Move magnet
B
Body weight (g)
Time (days)
Cell injection + Magnet
Remove magnet
Tumor volume (mm³)
Non-labeled EGFR CAR T-cell + magnet
γ-Fe2O3 labeled EGFR CAR T - magnet
γ-Fe2O3 labeled EGFR CAR T + magnet
C
D3
D6
D9
D13
γ-Fe2O3 labeled CAR T-cells with magnet
γ-Fe2O3 labeled CAR T-cells without magnet
Non-labeled CAR T-cells with magnet
Sagittal
Coronal
2 mm
D
Total volume of signal voids (in voxel)
Volume of signal voids > 100 voxels (in voxel)
Volume of signal voids < 100 voxels (in voxel)
Non-labeled CAR T-cell + magnet
γ-Fe2O3 labeled CAR T-cell - magnet
γ-Fe2O3 labeled CAR T-cell + magnet
Time (days)
***

Figure 7. A) Schematic representation outlining the key steps in the animal experiment protocol, alternating High-Resolution (HR) tumor imaging, and whole-body (WB) MR imaging. B) Mice body weight and tumor growth over time in the different groups. C) Representative longitudinal high resolution tumor monitoring obtained from MR scans, presented as minimum intensity projections of a 500 µm thick volume of sagittal or coronal sections, at day 3, day 6, day 9 and day 13. Scale bar corresponds to 2 mm. D) Quantification of the total volume (in number of voxels) of signal voids averaged for the different mice of each group at the different time points (left), of the volume of signal voids with more than 100 voxels (middle), and of the volume of signal voids with less than 100 voxels. N=3 mice per group; values are presented as mean ±SD. ***p<0.001 (One-way ANOVA).

As MRI longitudinal follow-up suggests the magnet induced early accumulation of γFe_2O_3 IONP-labeled EGFR CAR T-cells in the tumor between day 3 and day 7 post-injection (**Figure 7**), we therefore decided to carry out a complementary short-term *in vivo* experiment to confirm this hypothesis, comparing the effect of the magnet on the infiltration of the labeled EGFR CAR T-cells as well as UNT T-cells. Mice were sacrificed on day 4 after cell administration and tumors were analyzed by flow cytometry (**Figure 8B**).

Ex vivo results show an enhanced accumulation of CD3+ T-cells at tumor sites at day 4 in mice exposed to the magnet and injected with labeled T-cells in comparison to control groups without magnet or without IONP label. This confirms the HR-MRI *in vivo* quantification of hypointense signal regions, indicating magnet-enhanced tumor accumulation at this early time point. In addition to confirming *in vivo* longitudinal MRI results, an additional group was investigated to assess the magnetic attraction effect on UNT T-cells. Importantly, we observed similar tumor infiltration of the labeled UNT- T-cells and EGFR CAR-T-cells at day 4 when the magnet was present (**Figure 8B** and **8C**). This finding confirms that the active T-cell

accumulation in the tumor that is driven by the magnet at day 4 is not specific to the expression of the CAR on T cells.

Overall, we demonstrated that T-cell attraction, activated on demand by the application of a magnet, can play a critical cell-guiding role in facilitating the accumulation of T-cells towards tumor sites and change the spontaneous pace of T-cell trafficking after intravenous administration. Remarkably, the early infiltration of EGFR CAR T-cells in the tumor, mediated by magnetic guidance, ultimately contributes to an improved anti-tumor immune effect of CAR T therapy, with the potential to overcome solid tumor's resistance to cellular immunotherapy in clinical practice. The procedure described herein relies on a single procedure to immobilize the magnet, thereby reducing patient stress and minimizing repetitive invasive medical interventions. This approach therefore would present the key advantage allowing patients to maintain a normal lifestyle throughout the magnetic activation period. Moreover the magnetic labeling procedure of CAR T-cells described herein is straightforward, easily scalable and could be integrated in the autologous CAR T-cells manufacturing workflow without substantial additional costs or time-consuming procedures. As cost and time of manufacturing are major bottlenecks for the democratization of autologous CAR T therapy, it is a significant advantage in regards to more sophisticated procedures. Finally, the MRI real-time tracking of CAR T cells distribution might help to refine therapeutic procedures by detecting on-target as well as off-target T-cell accumulation with the potential to prevent side effects and inefficient use of treatment in resistant tumors.

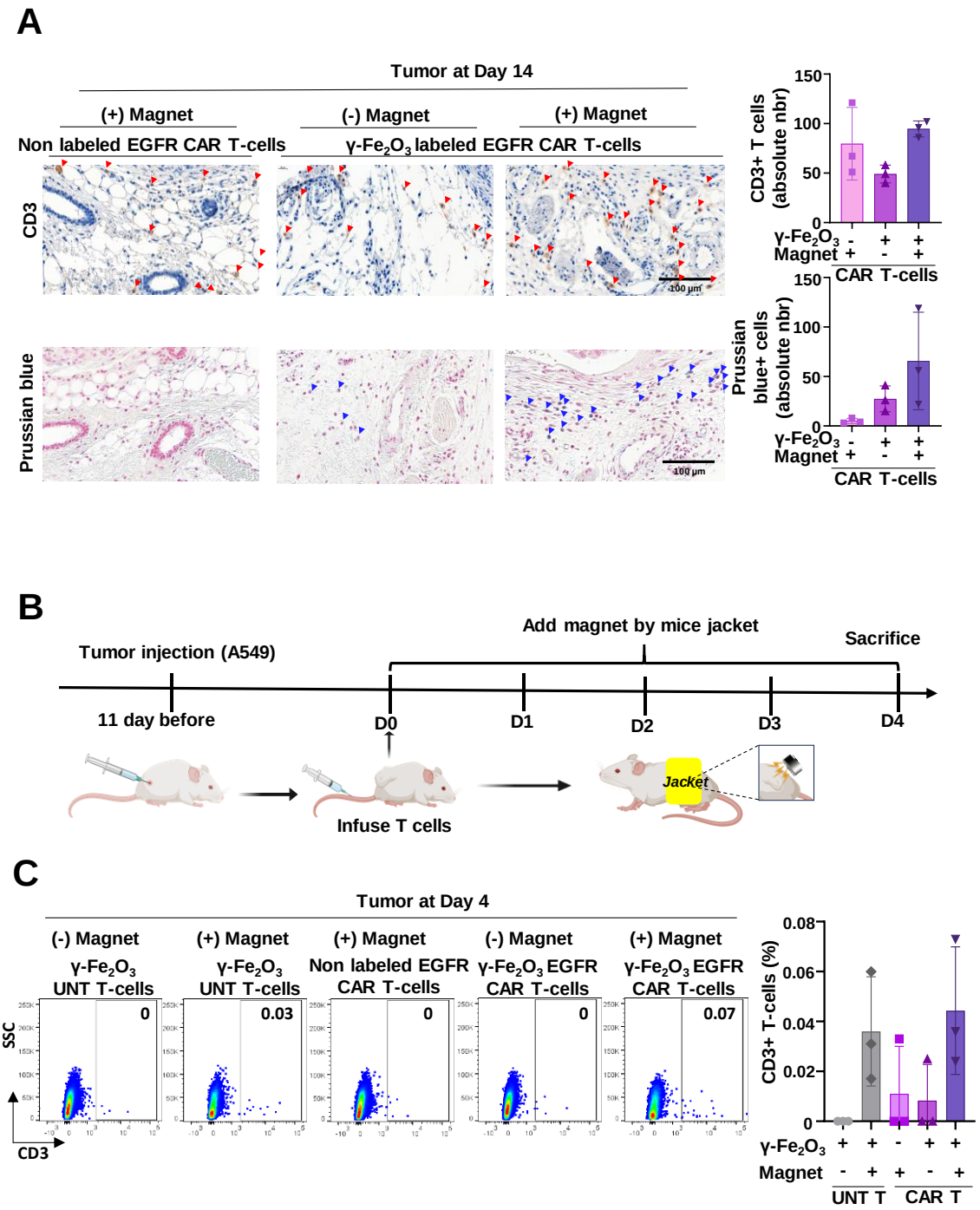

Figure 8. A) Representative anti-CD3 and Prussian blue staining on histological slices of tumors obtained after MRI monitoring and sacrifice at day 14 post T-cell injection in different groups with and without magnet. On the right, absolute quantification of the number of positive CD3 cells (red arrows on the histological slices) and positive Prussian blue cells (blue arrows). The scale bar is 100 µm. N=3 mice per group; values of n=3 images per animal are presented as mean ±SD. B) Schematic representation outlining the key steps in the animal experiment

protocol to validate T-cell accumulation at day 4 post T-cell injection using a magnet. C) Flow cytometry was performed to assess the expression of CD3 in tumor (left). The quantification of the percentage of these subsets is presented on the right. N=3 mice per group.

3. Conclusion

Our study addresses two critical clinical challenges associated to CAR T-cell therapy in solid tumors: the necessity for longitudinal *in vivo* spatio-temporal monitoring of the cell therapy with a clinical imaging method, and the requirement of an efficient infiltration of CAR T-cell within solid tumor. The rapid and simple intracellular labeling of CAR T cell with green, biodegradable and scalable iron oxide nanoparticles, that do not affect any of the CAR T-cell functionalities in vitro and in vivo in our preclinical model, offer the double possibility of MRI monitoring as companion test for cell therapy and of remotely-activated physical guidance of the T-cells at the tumor site to enhance their antitumor efficacy. These key elements represent a dual-pronged strategy for refining CAR T-cell-based therapeutic interventions, which could readily be implemented in clinics, as they do not require unconventional and/or sophisticated devices for magnetic guidance or imaging. Importantly, the intracellular iron oxide labeling procedure, allowing imaging as well as physical guidance of T cell, is independent of any antigen or TCR signaling pathway, so that it can be easily combined with any type of CAR or TCR targeting strategy of tumor cells.

Our work first demonstrates a noninvasive, clinically available and reliable real-time MR imaging technique, which allows the monitoring of effector immune cells trafficking and local tumor action, as well as enables the evaluation of IONP-labeled T-cells biodistribution, migration, and fate in a non-invasive manner. Importantly, we found that labeling T-cells with simple citrate-coated IONPs did not affect their immune functions and preserved EGFR-directed specificity and activation of EGFR CAR T against EGFR-expressing human lung

tumor xenograft in mice. Indeed our study uniquely compared the migration and biodistribution of EGFR-directed CAR T-cells with that of non-transduced T-cells by means of a longitudinal MRI follow up in the same animal for more than two weeks after cellular adoptive transfer. Our study highlights the specific dynamic behaviour of EGFR directed CAR T-cells in comparison to the naive T cells to migrate to and to attack EGFR-expressing solid tumors. The MRI discernible difference in the kinetics of spleen transit and subsequent tumor infiltration resulted in enhanced tumor penetration and antitumor efficacy for EGFR CAR T-cells. Such follow up could be implemented in preclinical and clinical trials for early assessment of the T cells access to the tumor in the weeks after administration and eventual comparison of different CAR or TCR (or their combination) designed to recognize and attack tumor cells. MRI monitoring of labeled T-cells in patients would provide a companion tool to document the distribution and killing effects of T-cells and their specificity to penetrate tumors while sparing healthy organs.

Moreover, we demonstrate that the same magnetic labeling of CAR T that is useful for non-invasive MR imaging, could be harnessed to modulate the biodistribution and fate of T-cells and enhance their anti-tumor efficacy through the simple application of a magnet, placed over the solid tumor's site during and in the first days following CAR T-cells administration. MRI follow up uniquely demonstrates the effect of the magnet on the kinetic of T-cell accumulation in the tumor, showing that the physical magnetic attraction soon after intravenous administration of the IONP-labeled T-cells can accelerate the infiltration of T-cells to the tumor in a way that is agnostic to the tumor antigen. Altogether, our strategy can combine the advantages of antigen specific targeting and physical guiding of T cell, each of them having different kinetics, to promote T cell infiltration and antitumor properties, while reducing the side effects.

Our clinically relevant strategy holds the potential to overcome on-target/off-tumor toxicity

by magnetically guiding CAR-T cells toward spatially restricted tumor distributions, and holds therapeutic advantages because it could be easy to deploy by medical practitioners and would be patient friendly, as the magnet could be placed non-invasively and patient could maintain a normal lifestyle during the magnetic guiding process.

Our cell tracking approach, which utilizes safe, degradable and intracellularly-recyclable iron-based nanoparticles, can advance both adoptive cell transfer−based cancer immunotherapy and other cell-based therapy approaches and could become part of next-generation imaging and therapeutic cell delivery techniques.

4. Experimental section

Chemical materials

Ferrous chloride ($FeCl_2$, ⩾98%), nitric acid (HNO_3, 65.0 – 68.0%), ferric chloride (FeCl3, $FeCl_3 \cdot 6H_2O$, ⩾98%), sodium citrate tribasic dihydrate ($C_6H_5Na_3O_7 \cdot 2H_2O$, ⩾99.0%), Iron(III) nitrate nonahydrate ($Fe(NO_3)_3 \cdot 9H_2O$, ⩾98%), absolute ethanol (C_2H_6O, ⩾99.7%), sodium acetate ($CH_3COONa \cdot 3H_2O$), and diethylene glycol ($C_4H_{10}O_3$) were procured from Sigma-Aldrich, ensuring a minimum purity of 98%. Deionized water was utilized following a rigorous purification process.

Synthesis of water-dispersible γ-Fe_2O_3 IONPs by coprecipitation method

Superparamagnetic γ-Fe_2O_3 IONPs were synthesized via a coprecipitation method.[43] The synthesis involved the following steps: first, magnetite (Fe_3O_4) particles were prepared by alkaline co-precipitation of a stoichiometric mixture of ferrous and ferric chlorides ($FeCl_2$ and $FeCl_3$). Initially, $FeCl_3 \cdot 6H_2O$ (15g in 107 mL of water, 0.055 mol) and $FeCl_2 \cdot 4H_2O$ (10.1 g in 17.75 mL of water, 0.051 mol) were dissolved separately in two beakers under continuous stirring at room temperature. A solution of concentrated 37% vol hydrochloric acid (3.5 mL) was then added to the $FeCl_2 \cdot 4H_2O$ solution, resulting in a light green mixture that was stirred

for 10 min. The ferrous chloride solution was subsequently added to the ferric chloride solution under stirring, causing the mixture to immediately turn light brown. After that, 35 mL of concentrated ammonia solution (32%vol) was added to the mixture and stirred for 15 min at room temperature before decantation on a magnetic plate for approximately 3 minutes. The resulting precipitate was washed with ultrapure water to remove impurities, followed by the addition of 125 mL of an 8%vol nitric acid solution and stirring for 15 minutes. The magnetic NPs were then decanted on a magnetic plate. This co-precipitation step ($2Fe^{3+}+Fe^{2+}+8OH^{-}$——$Fe_3O_4+4H_2O$) leads to a black precipitate composed of negatively charged magnetite particles. The precipitate was then oxidized in maghemite (γ-Fe_2O_3) by hot oxidation with ferric nitrate ($Fe(NO_3)_3$). Note that maghemite is chemically more stable than magnetite which partially oxidizes over time. For this, a boiling solution of ferric nitrate (19.25 g of ferric nitrate nonahydrate in 28.5 mL of water) was added to the Fe_3O_4 NPs precipitate, and the resulting mixture was stirred at 90°C for 25 minutes before decantation on a magnetic plate. The precipitate was washed three times with acetone and two times with ether before being dispersed in 35 mL of water. Any residual ether was removed by heating at 40°C for 15 minutes. Subsequently, 1 g of sodium citrate was added to the ferrofluid solution under stirring, followed by heating at 80°C and stirring for 15 minutes. The mixture was then precipitated with 35 mL of acetone and decanted on a magnetic plate. After two cycles of washing with acetone and ether, the precipitate was dispersed again in a determined volume of water based on the desired particle fraction (approximately 25 mL of water for 20% wt). Any residual ether was eliminated by heating at 40°C for 20 minutes, resulting in an aqueous ferrofluid of γ-Fe_2O_3 nanoparticles, negatively charged with sodium counterions.

IONP characterization

For transmission electron microscopy (TEM) analyses, a 3 µL drop of the above IONPs suspension (2 mg/mL) was placed on a carbon-coated copper grid for 1 min, then the excess

liquid was removed on filter paper and the solvent was allowed to dry at room temperature. Image analysis was performed using ImageJ software. Dynamic light scattering (DLS) for colloidal characterization was carried out using a Nano Sizer ZS (Malvern). We analyzed a suspension of IONPs in water (1 mg/mL) to measure hydrodynamic size. Electron Paramagnetic Resonance (EPR) was used to investigate the ferrimagnetic resonance of IONP and quantify the IONPs in suspension and cells as previously described by measuring the integrated absorption signal (double integration method). We performed a calibration assay with the IONPs used in this study at different iron concentrations in a 2 µL volume. This calibration curve was used to quantify IONPs in cells. EPR measurements were performed using a Bruker Elexsys 500 EPR spectrometer (Bruker, Wissembourg, France), operating at X-band (9.85 GHz) and equipped with a SHQ high-sensitivity cavity. Typical settings used were: microwave power, 1 mW; modulation frequency, 100 kHz; modulation amplitude, 1 mT; receiver gain, 45 dB; time constant, 40.96 ms; conversion time, 40.96 ms; data points, 2048; sweep width, 700 mT; sweep time, 83.89 s. Data acquisition and processing were performed using Bruker Xepr software.

T-cell line Culture

Human T-cell lines (CEM and J77 T-cells) were cultured with RPMI 1640 medium with 10% fetal bovine serum (FBS), 1% penicillin/streptomycin (P/S), and incubated at 37 °C with 5% CO_2 and 90% relative humidity.

Primary T-cell isolation

Human studies were carried out according to French law on biomedical research and to principles outlined in the 1975 Helsinki Declaration and its modification. T-cells were isolated from blood of healthy donors obtained from the *Etablissement Français du Sang* in Rungis, under agreement 18/EFS/030, including informed consent for research purposes. Samples were anonymous and not associated with any personal data. The human peripheral blood mononuclear cells (PBMC) were purified using a density gradient medium (Lymphoprep™).

T-cells were then isolated from PBMC using a negative selection approach using the Pan T-cell Isolation Kit (Miltenyi) as follows: PBMC labeled with antibodies and beads from Pan T-cell Isolation Kit were added to the LS column (Miltenyi) to achieve magnetic depletion of labeled cells (not-T cells) and isolation of unlabeled cells (T-cells). T-cells were then stimulated at 2×10^6/mL in culture medium (RPMI 10%FBS and 1%PS) with 100U/mL of IL-2 and 1/200 of T-cell TransAct™ in a 24-well plate. The plate was incubated for 3 days at 37°C 5% CO_2. T-cells were split every 2 days in a culture medium with 100U/mL of IL-2 during 1 week.

Generation of EGFR CAR T-cells

The plasmid construct encoding under EF-1alpha promoter for second-generation anti-EGFR CARs (SCFV from Nimotuzumab antibody), CD8 hinge transmembrane domains, 4-1BB costimulatory, CD3z signalling domains followed by *Enhanced Green Fluorescent Protein* (EGFP), to estimate the percentage of transduction, and was generated by Creative Biolabs Inc. Lentiviral particles were produced in HEK293T packaging cell line. Activated T-cells were then transduced at day 1 using a MOI (Ratio of viral particles to the number of target cells) of 5. Cells were maintained at 2×10^6 cells / mL until day 12 in RPMI 10% FBS 1% PS and 10 ng/mL of IL7 and IL15. In experiments involving EGFR CAR T cells, the control groups consist of untransduced T-cells (UNT T-cell), which are activated and stimulated in the same manner as CAR T cells but remain non transduced by lentiviral particles.

T-cell labeling with IONPs and cell viability test

T-cells were cultured in 96-well plates at a concentration of 2×10^5 cells/well and incubated with IONPs at varying concentrations (0-400 µg/mL) dispersed in RPMI 1640 medium without FBS and PS and supplemented with 5mM sodium citrate, for 2 or 24 hours and then washed to discard residual IONP. For mitochondrial metabolic activity test, T-cells were incubated with Alamar blue solution (10% v/v) (Thermo Fisher Scientific, MA, USA) in phenol red-free media 10% for 2 to 4 hours until the medium color transitioned from blue to pink. The conditioned

medium was then transferred to a fresh plate for measuring absorbance at 530 nm using a microplate reader.

EPR quantification of IONP cellular uptake

T-cells (1×10^6 cells/well) were incubated with two concentrations of γ-Fe_2O_3 NPs (50, 100 μg/mL) in RPMI 1640 without FBS and PS supplemented with 5 mM sodium citrate in 12-well plates. Following incubation, cells underwent triple washes with PBS to eliminate residual nanoparticles. The cell count was determined after resuspension in 10 μL PBS. Subsequently, 2 μL of the solution was subjected to EPR measurement as described above, and results were analyzed using EPR software, using the double integral method to quantify the IONP mass in the sample. Besides, T-cells from two additional donors (1×10^6 cells/well) were incubated with γ-Fe_2O_3 NPs (50 μg/mL) in RPMI 1640 without FBS and PS supplemented with 5 mM sodium citrate in 12-well plates at two different temperature (4°C and 37°C) for 30 min, 2 h and 4 h. After incubation, EPR measurements were performed as described above.

T-cell proliferation

CEM or J77 T-cells at a concentration of 1×10^6 cells per mL were incubated with different concentrations of IONPs (10-200 μg/mL) for 2 hours in 12-well plates within a 5% CO_2 atmosphere at 37°C. Then, cell number and viability assessments were quantified by NucleoCounter NC200 (ChemoMetec) analysis at specific intervals (day 1, 3, 5, 7, and 9) to evaluate the proliferative rate.

To monitor primary T-cell proliferation, IONPs labeled T-cells were washed in PBS and stained by Cell Trace™ Violet (dilution: 1/5000 in fresh PBS) at the concentration of 1×10^6 per mL for 3 min at 4°C. After washing, T-cells were resuspended in culture media at 2×10^6 per mL and stimulated with T-cell TransAct™ (1/200) and 10 ng/mL of IL-7 and IL-15 in RPMI (10% FBS, 1% PS) in a 24-well plate. Activated T-cells were harvested at Day 0, 2, 5, and 7. Proliferating cells and phenotypes were monitored by Flow cytometry.

Flow cytometry analyses

To assess T-cell phenotype, T-cells were first stained with Live/Dead^{TM} (1/1000) for 30 min at 4°C and washed with PBS 2% FBS. Then, T-cell phenotypes were assessed using 1/200 of anti-CD3, anti-CD4, anti-CD8, anti-CD25, anti-CD69, anti-CD62L and anti-CD45RO (Milteniy, Biolegend) during 20min at 4°C. The expression of CAR is assessed by evaluating EGFP expression, as well as by biotinylated anti-CAR EGFR labeling at a 1/50 dilution for 30 minutes at 4°C, followed by secondary labeling with streptavidin APC at a 1/100 dilution for 30 min at 4°C. T-cells were then washed in PBS 2% and the phenotypes were measured by Flow Cytometer (LSR II-Fortessa, BD). Data were analyzed using FlowJo software.

T-cell migration assay

Transwell assay: T-cell transmigration assays were conducted using 24-mm transwell plates with 3-µm pore size (Costar). The lower wells were preloaded with the cytokine CXCL12 (SDF1, 100 ng/mL) for 30 minutes at 37°C 5%CO_2. Subsequently, T-cells (0.5×10^6/well) were exposed to 50 µg/mL of γ-Fe_2O_3 IONPs for 2 hours in RPMI supplemented with 5 mM sodium citrate. Following incubation, the cells were thoroughly washed with PBS. The labeled T-cells resuspended in RPMI 1640 medium supplemented with 10% FBS and 1% PS were then introduced into the upper chamber of the transwell plate. The number of T-cells that migrated into the lower chamber was analyzed within a 24-hour period.

Collagen gel assay: γ-Fe_2O_3 labeled T-cells were stained with CellTrace™ Calcein Green (dilution 1/1000) and unlabeled T-cell were stained with CellTrace™ Calcein Red (dilution 1/1000) for 20 min at room temperature, respectively. T-cells were then washed with culture media and plated on a 6 channel IBIDI µ-Slide in 2 mg/mL of collagen gel and incubated for 1 hour at 37°C, 5%CO_2. Migrating T-cells were recorded on an inverted widefield microscope (Nikon Eclipse TE2000-U) preheated at 37°C with a time interval of one picture every 30 sec during 7.5 min and a Z-stack of 15 µm. T-cell tracks were assessed with Image J.

In vitro High-Resolution MRI

High resolution MRI was conducted on 1.5 mL Eppendorf tubes with 500 µL 0.3% agarose gel containing dispersed γ-Fe_2O_3 IONP labeled T-cells. T-cells at a concentration of 10^6 UNT T-cells/mL were incubated with varying concentrations of γ-Fe_2O_3 NPs (10-100 µg/mL) for a duration of 2 hours in RPMI supplemented with 5 mM citrate. After 3 lavages with PBS to remove residual IONPs in the medium, IONP labeled T-cells with varying concentrations of IONPs (15000 cells per tube) or different T-cell numbers (5000, 10000, 15000 per tube) labelled with γ-Fe_2O_3 NPs at 50 µg/mL were then gently dispersed in 500 ml of 0.3% low-melting-point agarose solution at 40 °C and cooled at 4 °C until jellification, in presence or absence of the magnet. Control was agarose gel with 15000 non-labeled cells.

MRI was performed on the Biospec 47/40 USR Scanner (40 cm bore actively shielded 4.7 T magnet) interfaced to ParaVision software (both provided from Bruker Biospin GmbH, Rheinstetten, Germany) at the imaging facility of the Université Paris Cité: Plateforme Imageries du Vivant (PARCC-HEGP, INSERM UMR 970, Paris, France). High-resolution-MRI was achieved using the cryogenic surface probe (CryoProbe™, Bruker). Three-dimensional (3D) isotropic susceptibility-weighted gradient echo sequence with RF spoiling, TR/TE = 39/9 ms, flip angle=20°, NEX=1, FOV: 10x10x10 mm, matrix: 200x200x200 and a voxel resolution of 50x50x50 μm^3 was used. ImageJ software (version 1.54f) was used for the quantification of hypo-intense MRI signal voids corresponding to single T-cells on each sequential MR slice, on which a threshold was applied, a binary image was formed and the dots were counted with the Analyze Particle function.

Magnetic attraction assay

γ-Fe_2O_3 labeled T-cells and unlabeled T-cells were stained with CellTrace™ Calcein green and red respectively, and washed in culture medium. T-cells (0.5×10^6) were plated on a 6 channel IBIDI µ-Slide. γ-Fe_2O_3 labeled T-cells and unlabeled T-cells displacement were first acquired

in culture medium without magnet on an inverted microscope with a time interval of one picture every 3 sec during 1 min. The magnet was then placed on the 6 channel IBIDI µ-Slide and T-cell displacements were recorded with the same parameters (Time interval: 3 sec; 20 times). Images were analysed with ImageJ and T-cell tracks were quantified with R studio.

The magnet T-cell attraction experiment was also performed in 0.3% agarose gel as described above.

Intracellular calcium measurement

To measure intracellular Ca^{2+} concentration, γ-Fe_2O_3 labeled or non-labeled CAR T-cells were stained with 1µM of Fura2 AM for 30 min at 37°C, 5% CO_2. T-cells were washed and resuspended in culture medium. Fura2-loaded T-cells ($0.5x10^6$) were added to A549 cell line cultured previously in a 6-channel IBIDI µ-Slide. Images were recorded every 10 sec at 350 and 380 nm using MetaFluor software. The change of the wavelength of excitation (from 380 nm to 340 nm) when cytosolic free Ca^{2+} binds to Fura-2 allows to obtain ratiometric Ca^{2+} measurement, i.e. the signal ratio between the wavelengths (F340/380) of free Ca^{2+} and bound Ca^{2+}. CAR T-cells were considered responsive when the amplitude of their responses reached at least twice that of the background.

Cytokine measurement

γ-Fe_2O_3 IONP labeled T-cells and non-labeled T-cells were added to A549 tumor cell line pre-plated at $0.5x10^6$ in a 48-well plate. Supernatants were recovered and freezed 24 hours after co-culture. Cytokines were measured using LEGENDplex™ Human CD8/NK Panel (13-plex) w/ VbP V02 (Biolegend).

Tumor spheroid attack experiment

A549 cells were cultured in cell repellent round-bottom 96-well plates (Greiner Bio-one) at a seeding density of 2500 cells per well. Subsequently, the plates were placed in the CellInsight CX7 LZR HCS-platform (Thermo Scientific) incubator set at 37°C with 5% CO_2 and 70%

humidity for 4 days, during which images were captured at 4-hour intervals. Following this incubation period, the resultant A549 cell aggregates were identified as tumor spheroids. Then, γ-Fe_2O_3 labeled or non-labeled UNT T-cells or EGFR CAR T-cells, previously stained with CellTrace™ Calcein green, were introduced into the well at a predetermined ratio of 10:1, equating to 25 000 T-cells per well. The entire well plate was subsequently transferred to the CellInsight system and maintained in a controlled environment at 37°C with 5% CO_2 for an additional 5 days. Image acquisition occurred at regular intervals of 4 hours throughout this duration, with the following acquisition parameters: 10x objective and camera binning 2x2, Z-stack (15 µm-step, 11 steps) of every spheroid, Channel 1: brightfield with amber (590 nm) illumination at 100%, gain 2, and 15 ms exposure, Channel 2: green epi-fluorescent with illumination/filter setup 488LZR_BGS_BGS, illumination at 100%, 70 µm spinning disk pinhole size, gain 2, and 150 ms exposure.

Deidentified human skin primary fibroblasts were obtained with consent from a healthy individual with no known metabolic disease at Necker–Enfants Malades Hospital. These fibroblasts were cultured in Dulbecco-modified Eagle medium (DMEM) high glucose supplemented with 1% PS and 10% FBS. All experiments have been done with cells between 15 and 19 passages. A549 cells mixed with the above human fibroblast cell at the number ratio is 4:1 (Total cell number is 2500 for each well) were cultured in cell-repellent round-bottom 96-well plates. Subsequently, tumor spheroid experiment was performed as described above.

Animal experiments

NOD.Cg-Prkdc(scid)Il2rg(tm1Wjll)/SzJ (abbreviated NSG) immunodeficient mice (The Jackson Laboratory, Bar Harbor, ME, USA, 005557) were housed in pathogen-free condition at Cochin Institute Animal Facility. The mice protocol for CAR-T has been approved by Université Paris Cité (CEEA 17-039) and the French Ministry of Research (APAFiS #15076).

A549 cells ($5x10^6$ in 100 µL PBS) were injected subcutaneously into the flank of NSG mice

and handled according to the recommendations of the CNB-CSIC institutional Ethics Committee. Approximately 12 days post-injection, EGFR CAR T-cells, or untransduced UNT T-cells, with or without γ-Fe_2O_3 IONPs label, were administrated intravenously ($1x10^6$ T-cells (or $2.5x10^6$ cells for the last short term animal experiment) in 200 µL PBS) into the NSG mice tail. Tumor burden was measured by the caliper every day until sacrifice on day 14. Tumor volume was calculated by the formula: tumor volume = (length of the tumor) × (width of the tumor)^2/2. To evaluate the magnetic guidance of labelled T-cells *in vivo*, a magnet was added to the tumor mass for 4 to 5 days using a mouse jacket. Mice organs were harvested to evaluate T-cell and IONPs infiltration and toxicity by immuno-cytometry and histology (H&E, Prussian blue staining) at the end of the experiment.

In vivo longitudinal MRI monitoring

As for *in vitro* imaging, *in vivo* longitudinal MRI monitoring was performed on the Biospec 47/40 USR Scanner on the imaging facility of the Université Paris Cité. High-resolution-MRI was achieved using the cryogenic surface probe (CryoProbe™, Bruker) placed on the tumor mass using a 3D isotropic T2*-weighed sequence with RF spoiling, TR/TE = 39/9 ms, flip angle=20°, NEX=1, FOV: 14x13x12 mm, matrix: 280x260x240, resolution: 50x50x50 µm^3 with a zero filling interpolation of 1,34 and an acquisition time of 25 min 14s. The number and volume of hypo-intense signal regions was quantified manually over the entire tumor region by detecting the corresponding hypo-intense signal areas in each sequential slice using ImageJ software, by which a threshold was applied and a binary image was formed.

Mouse whole body MRI was performed using a 35 mm inner diameter resonator and 2D FLASH sequence with TR/TE = 300/3 ms, flip angle=30°, NEX=8, 41 slices, FOV: 30x30 mm, matrix : 256x256, resolution : 117x117 micrometers with a zero filling interpolation of 1,34 and acquisition time : 7 min 41s. For whole body MRI, the signal was measured in different organs of interest and normalized to a water tube signal reference positioned near the mouse.

Statistical Analysis

For tumor spheroids, tumor size analysis was performed using Icy software. In the analysis of in vitro MR imaging, the number of MRI cell signal points was quantified using ImageJ. Additionally, ImageJ/Fiji was employed to quantify grayscale values for in vivo MR imaging, with water as the reference standard. The corresponding figure was generated and analyzed using Origin 8.0. Statistical analysis was performed using the Origin 8.0 or GraphPad Prism 8.0 program (GraphPad Software, Inc., La Jolla, CA, USA), and data were presented as mean ± SD or mean ± SEM, as specified in the concerned figure caption. The p values were calculated by one-way ANOVA and p values were indicated as follows: *$p<0.05$, **$p<0.01$, ***$p<0.001$, ****$p<0.0001$.

Supporting Information

Supporting Information is available from the Wiley Online Library or from the author.

Acknowledgments

This research was supported by China Scholarship Council (HC, NO. 202006630008), ITMO Cancer of Aviesan within the framework of the 2021-2030 Cancer Control Strategy, on funds administered by Inserm (n°21CP074-00), by the French Ligue Nationale contre le Cancer (Equipes labellisées) (ED), by the IdEx Université Paris Cité, ANR-18-IDEX-0001 (IVETh plateform), by the Region Ile de France under the convention SESAME 2019 - IVETh (EX047011) (IVETh plateform), by the Region Ile de France and Banque pour l'Investissement (BPI) under the convention Accompagnement et transformation des filières projet de recherche et développement N° DOS0154423/00 & DOS0154424/00 (IVETh platform), and Agence Nationale de la Recherche through the program France 2023 "Intégrateur biotherapie-bioproduction" (ANR-22-AIBB-000). We are grateful to Kelly Aubertin for fruitful discussion, to Sonia Lajnef for help in EPR experiments and the staff of CYBIO, PIV, and HistIM facilities

of the Cochin Institute for their advice during this study.

We acknowledge the analysis platform core facility of BioMedTech Facilities INSERM US36 | CNRS UAR2009 | Université Paris Cité, the ImagoSeine core facility of the Institut Jacques Monod, member of the France BioImaging infrastructure (ANR-10-INBS-04) and GIS-IbiSA, the EPR core facility (UMR8601/CNRS/Université Paris Cité) and the HistIM facility at Cochin Institute, Université Paris Cité.

Conflicts of interest

There are no conflicts of interest to declare.

References

1. Godinho-Silva C, Cardoso F, Veiga-Fernandes H. Neuro–immune cell units: a new paradigm in physiology. *Annual review of immunology* 2019; **37**(1): 19-46.
2. Mellman I, Chen DS, Powles T, Turley SJ. The cancer-immunity cycle: Indication, genotype, and immunotype. *Immunity* 2023; **56**(10): 2188-205.
3. Wu L, Wei Q, Brzostek J, Gascoigne NR. Signaling from T cell receptors (TCRs) and chimeric antigen receptors (CARs) on T cells. *Cellular & Molecular Immunology* 2020; **17**(6): 600-12.
4. Fujiwara K, Tsunei A, Kusabuka H, Ogaki E, Tachibana M, Okada N. Hinge and transmembrane domains of chimeric antigen receptor regulate receptor expression and signaling threshold. *Cells* 2020; **9**(5): 1182.
5. Helmy KY, Patel SA, Nahas GR, Rameshwar P. Cancer immunotherapy: accomplishments to date and future promise. *Therapeutic delivery* 2013; **4**(10): 1307-20.
6. Sadelain M, Brentjens R, Rivière I. The basic principles of chimeric antigen receptor design. *Cancer discovery* 2013; **3**(4): 388-98.
7. Ellis GI, Sheppard NC, Riley JL. Genetic engineering of T cells for immunotherapy. *Nature Reviews Genetics* 2021; **22**(7): 427-47.
8. Martinez M, Moon EK. CAR T cells for solid tumors: new strategies for finding, infiltrating, and surviving in the tumor microenvironment. *Frontiers in immunology* 2019; **10**: 128.
9. Rodriguez-Garcia A, Palazon A, Noguera-Ortega E, Powell Jr DJ, Guedan S. CAR-T cells hit the tumor microenvironment: strategies to overcome tumor escape. *Frontiers in immunology* 2020; **11**: 1109.
10. Hong M, Talluri S, Chen YY. Advances in promoting chimeric antigen receptor T cell trafficking and infiltration of solid tumors. *Current Opinion in Biotechnology* 2023; **84**: 103020.
11. Flugel CL, Majzner RG, Krenciute G, et al. Overcoming on-target, off-tumour toxicity of CAR T cell therapy for solid tumours. *Nature Reviews Clinical Oncology* 2023; **20**(1): 49-62.
12. Feng K, Guo Y, Dai H, et al. Chimeric antigen receptor-modified T cells for the immunotherapy of patients with EGFR-expressing advanced relapsed/refractory non-small cell

lung cancer. *Science China life sciences* 2016; **59**: 468-79.
13. Ott PA, Dotti G, Yee C, Goff SL. An update on adoptive T-cell therapy and neoantigen vaccines. *American Society of Clinical Oncology Educational Book* 2019; **39**: e70-e8.
14. Guo Y, Feng K, Liu Y, et al. Phase I study of chimeric antigen receptor–modified T cells in patients with EGFR-positive advanced biliary tract cancers. *Clinical Cancer Research* 2018; **24**(6): 1277-86.
15. Liu Y, Guo Y, Wu Z, et al. Anti-EGFR chimeric antigen receptor-modified T cells in metastatic pancreatic carcinoma: a phase I clinical trial. *Cytotherapy* 2020; **22**(10): 573-80.
16. Wang J, Chen J, Guo Y, Wang B, Chu H. Strategies targeting angiogenesis in advanced non-small cell lung cancer. *Oncotarget* 2017; **8**(32): 53854.
17. Xia L, Zheng Zz, Liu Jy, et al. EGFR‐targeted CAR‐T cells are potent and specific in suppressing triple‐negative breast cancer both in vitro and in vivo. *Clinical & Translational Immunology* 2020; **9**(5): e1135.
18. Nicolas-Boluda A, Vaquero J, Vimeux L, et al. Tumor stiffening reversion through collagen crosslinking inhibition improves T cell migration and anti-PD-1 treatment. *Elife* 2021; **10**: e58688.
19. Derynck R, Turley SJ, Akhurst RJ. TGFβ biology in cancer progression and immunotherapy. *Nature Reviews Clinical Oncology* 2021; **18**(1): 9-34.
20. Anderson KG, Stromnes IM, Greenberg PD. Obstacles posed by the tumor microenvironment to T cell activity: a case for synergistic therapies. *Cancer cell* 2017; **31**(3): 311-25.
21. Liu Y-T, Sun Z-J. Turning cold tumors into hot tumors by improving T-cell infiltration. *Theranostics* 2021; **11**(11): 5365.
22. Zhang J, Endres S, Kobold S. Enhancing tumor T cell infiltration to enable cancer immunotherapy. *Immunotherapy* 2019; **11**(3): 201-13.
23. Emami-Shahri N, Foster J, Kashani R, et al. Clinically compliant spatial and temporal imaging of chimeric antigen receptor T-cells. *Nature communications* 2018; **9**(1): 1081.
24. Mulazzani M, Fräßle SP, von Mücke-Heim I, et al. Long-term in vivo microscopy of CAR T cell dynamics during eradication of CNS lymphoma in mice. *Proceedings of the National Academy of Sciences* 2019; **116**(48): 24275-84.
25. Kiru L, Zlitni A, Tousley AM, et al. In vivo imaging of nanoparticle-labeled CAR T cells. *Proceedings of the National Academy of Sciences* 2022; **119**(6): e2102363119.
26. Bremer C, Ntziachristos V, Weissleder R. Optical-based molecular imaging: contrast agents and potential medical applications. *European radiology* 2003; **13**: 231-43.
27. Bulte JW, Douglas T, Witwer B, et al. Magnetodendrimers allow endosomal magnetic labeling and in vivo tracking of stem cells. *Nature biotechnology* 2001; **19**(12): 1141-7.
28. Karussis D, Karageorgiou C, Vaknin-Dembinsky A, et al. Safety and immunological effects of mesenchymal stem cell transplantation in patients with multiple sclerosis and amyotrophic lateral sclerosis. *Archives of neurology* 2010; **67**(10): 1187-94.
29. Hoehn M, Küstermann E, Blunk J, et al. Monitoring of implanted stem cell migration in vivo: a highly resolved in vivo magnetic resonance imaging investigation of experimental stroke in rat. *Proceedings of the National Academy of Sciences* 2002; **99**(25): 16267-72.
30. Bulte J, Zhang S-C, Van Gelderen P, et al. Neurotransplantation of magnetically labeled oligodendrocyte progenitors: magnetic resonance tracking of cell migration and myelination. *Proceedings of the National Academy of Sciences* 1999; **96**(26): 15256-61.
31. De Vries IJM, Lesterhuis WJ, Barentsz JO, et al. Magnetic resonance tracking of dendritic cells in melanoma patients for monitoring of cellular therapy. *Nature biotechnology* 2005; **23**(11): 1407-13.
32. Ahrens ET, Bulte JW. Tracking immune cells in vivo using magnetic resonance imaging. *Nature Reviews Immunology* 2013; **13**(10): 755-63.

33. Daldrup-Link HE, Golovko D, Ruffell B, et al. MRI of tumor-associated macrophages with clinically applicable iron oxide nanoparticles. *Clinical Cancer Research* 2011; **17**(17): 5695-704.
34. Hunger J, Schregel K, Boztepe B, et al. In vivo nanoparticle-based T cell imaging can predict therapy response towards adoptive T cell therapy in experimental glioma. *Theranostics* 2023; **13**(15): 5170.
35. Volatron J, Carn F, Kolosnjaj‐Tabi J, et al. Ferritin protein regulates the degradation of iron oxide nanoparticles. *Small* 2017; **13**(2): 1602030.
36. Kolosnjaj-Tabi J, Lartigue L, Javed Y, et al. Biotransformations of magnetic nanoparticles in the body. *Nano Today* 2016; **11**(3): 280-4.
37. Wilhelm C, Bal L, Smirnov P, et al. Magnetic control of vascular network formation with magnetically labeled endothelial progenitor cells. *Biomaterials* 2007; **28**(26): 3797-806.
38. Cheng K, Li T-S, Malliaras K, Davis DR, Zhang Y, Marbán E. Magnetic targeting enhances engraftment and functional benefit of iron-labeled cardiosphere-derived cells in myocardial infarction. *Circulation research* 2010; **106**(10): 1570-81.
39. Riegler J, Wells JA, Kyrtatos PG, Price AN, Pankhurst QA, Lythgoe MF. Targeted magnetic delivery and tracking of cells using a magnetic resonance imaging system. *Biomaterials* 2010; **31**(20): 5366-71.
40. Muthana M, Kennerley AJ, Hughes R, et al. Directing cell therapy to anatomic target sites in vivo with magnetic resonance targeting. *Nature communications* 2015; **6**(1): 8009.
41. Tang X, Yang Y, Zheng M, et al. Magnetic–acoustic sequentially actuated CAR T cell microrobots for precision navigation and in situ antitumor immunoactivation. *Advanced Materials* 2023; **35**(18): 2211509.
42. Chaudeurge A, Wilhelm C, Chen-Tournoux A, et al. Can magnetic targeting of magnetically labeled circulating cells optimize intramyocardial cell retention? *Cell Transplantation* 2012; **21**(4): 679-91.
43. Massart R. Preparation of aqueous magnetic liquids in alkaline and acidic media. *IEEE transactions on magnetics* 1981; **17**(2): 1247-8.
44. Wilhelm C, Gazeau F. Universal cell labelling with anionic magnetic nanoparticles. *Biomaterials* 2008; **29**(22): 3161-74.
45. Smirnov P, Poirier‐Quinot M, Wilhelm C, et al. In vivo single cell detection of tumor‐infiltrating lymphocytes with a clinical 1.5 Tesla MRI system. *Magnetic Resonance in Medicine: An Official Journal of the International Society for Magnetic Resonance in Medicine* 2008; **60**(6): 1292-7.
46. Smirnov P, Lavergne E, Gazeau F, et al. In vivo cellular imaging of lymphocyte trafficking by MRI: a tumor model approach to cell‐based anticancer therapy. *Magnetic Resonance in Medicine: An Official Journal of the International Society for Magnetic Resonance in Medicine* 2006; **56**(3): 498-508.
47. Wilhelm C, Gazeau F, Bacri J-C. Magnetophoresis and ferromagnetic resonance of magnetically labeled cells. *European Biophysics Journal* 2002; **31**: 118-25.
48. Levy M, Luciani N, Alloyeau D, et al. Long term in vivo biotransformation of iron oxide nanoparticles. *Biomaterials* 2011; **32**(16): 3988-99.
49. Rock KL, Kono H. The inflammatory response to cell death. *Annu Rev Pathol Mech Dis* 2008; **3**: 99-126.
50. Miquel J. An update of the oxidation-inflammation theory of aging: the involvement of the immune system in oxi-inflamm-aging. *Current pharmaceutical design* 2009; **15**(26): 3003-26.
51. Fan X, Rudensky AY. Hallmarks of tissue-resident lymphocytes. *Cell* 2016; **164**(6): 1198-211.
52. Michalek RD, Rathmell JC. The metabolic life and times of a T‐cell. *Immunological*

reviews 2010; **236**(1): 190-202.
53. Raskov H, Orhan A, Christensen JP, Gögenur I. Cytotoxic CD8+ T cells in cancer and cancer immunotherapy. *British journal of cancer* 2021; **124**(2): 359-67.
54. De Rosa SC, Herzenberg LA, Herzenberg LA, Roederer M. 11-color, 13-parameter flow cytometry: identification of human naive T cells by phenotype, function, and T-cell receptor diversity. *Nature medicine* 2001; **7**(2): 245-8.
55. Rea I, McNerlan S, Alexander H. CD69, CD25, and HLA-DR activation antigen expression on CD3+ lymphocytes and relationship to serum TNF-α, IFN-γ, and sIL-2R levels in aging. *Experimental gerontology* 1999; **34**(1): 79-93.
56. Campbell DJ. Control of regulatory T cell migration, function, and homeostasis. *The Journal of Immunology* 2015; **195**(6): 2507-13.
57. Masopust D, Schenkel JM. The integration of T cell migration, differentiation and function. *Nature Reviews Immunology* 2013; **13**(5): 309-20.
58. Fernandis AZ, Cherla RP, Ganju RK. Differential regulation of CXCR4-mediated T-cell chemotaxis and mitogen-activated protein kinase activation by the membrane tyrosine phosphatase, CD45. *Journal of Biological Chemistry* 2003; **278**(11): 9536-43.
59. Wells A. EGF receptor. *The international journal of biochemistry & cell biology* 1999; **31**(6): 637-43.
60. Normanno N, De Luca A, Bianco C, et al. Epidermal growth factor receptor (EGFR) signaling in cancer. *Gene* 2006; **366**(1): 2-16.
61. Liu Y, Fang Y, Chen X, et al. Gasdermin E–mediated target cell pyroptosis by CAR T cells triggers cytokine release syndrome. *Science immunology* 2020; **5**(43): eaax7969.
62. Shao M, Teng X, Guo X, et al. Inhibition of calcium signaling prevents exhaustion and enhances anti‐leukemia efficacy of CAR‐T cells via SOCE‐calcineurin‐NFAT and glycolysis pathways. *Advanced Science* 2022; **9**(9): 2103508.
63. Li R, Ma C, Cai H, Chen W. The CAR T‐cell mechanoimmunology at a glance. *Advanced Science* 2020; **7**(24): 2002628.
64. Grilli F, Hassan EM, Variola F, Zou S. Harnessing graphene oxide nanocarriers for siRNA delivery in a 3D spheroid model of lung cancer. *Biomaterials Science* 2023; **11**(19): 6635-49.
65. Kolosnjaj-Tabi J, Wilhelm C, Clément O, Gazeau F. Cell labeling with magnetic nanoparticles: opportunity for magnetic cell imaging and cell manipulation. *Journal of nanobiotechnology* 2013; **11**(1): 1-19.
66. Tso R, Smith J, Doma K, Grant A, McEwen P. Clinical and patient-reported outcomes of medial stabilized versus non–medial stabilized prostheses in total knee arthroplasty: A systematic review and meta-analysis. *The Journal of Arthroplasty* 2021; **36**(2): 767-76. e2.
67. Mueller SN, Ahmed R. High antigen levels are the cause of T cell exhaustion during chronic viral infection. *Proceedings of the National Academy of Sciences* 2009; **106**(21): 8623-8.
68. Reddy UA, Prabhakar P, Mahboob M. Biomarkers of oxidative stress for in vivo assessment of toxicological effects of iron oxide nanoparticles. *Saudi journal of biological sciences* 2017; **24**(6): 1172-80.
69. Fahmy HM, Abd El‐Daim TM, Ali OA, Hassan AA, Mohammed FF, Fathy MM. Surface modifications affect iron oxide nanoparticles' biodistribution after multiple‐dose administration in rats. *Journal of Biochemical and Molecular Toxicology* 2021; **35**(3): e22671.
70. Mortezaee K. Immune escape: A critical hallmark in solid tumors. *Life sciences* 2020; **258**: 118110.

Table of contents entry

CAR T-cell therapy is a promising cancer treatment. However, its effectiveness in solid tumors is limited due to poor T-cell accumulation, infiltration, and retention at the tumor site. EGFR CAR T-cells were loaded with iron oxide nanoparticles and then intravenously injected into immune-deficient mice bearing subcutaneous human lung cancer cell-derived xenograft. The longitudinal tracking of CAR T-cells action, in comparison to untransduced T-cells, was performed in vivo using both whole-body and high-resolution MRI over 14 days. In addition, an external magnet was used to promote early CAR T-cell guidance to the tumor and enhance antitumor efficacy, in a clinically applicable strategy.

Huan Chen, Alice Machado, Dongjie An, Sonia Becharef, Gwennhael Autret, Dmitry Ayollo, Sarah Razafindrakoto, Philippe Nizard, Florent Carn, Yun Luo, Frédéric Pendino, Claire Mangeney, Jelena Kolosnjaj-Tabi, Emmanuel Donnadieu, Florence Gazeau

In vivo monitoring and magnetically-enhanced delivery of CAR T cells to solid tumor

ToC figure